Geochemistry Geophysics Geosystems G3
AN ELECTRONIC JOURNAL OF THE EARTH SCIENCES
Published by AGU and the Geochemical Society

Article
Volume 7, Number 1
25 January 2006
Q01004, doi:10.1029/2005GC001074
ISSN: 1525-2027

Mass transfer and fluid flow during detachment faulting and development of an oceanic core complex, Atlantis Massif (MAR 30°N)

Chiara Boschi, Gretchen L. Früh-Green, and Adélie Delacour
Department of Earth Sciences, ETH-Zurich, CH-8092, Zürich, Switzerland (frueh@erdw.ethz.ch)

Jeffrey A. Karson
Division of Earth and Ocean Sciences, Duke University, Durham, North Carolina 27708, USA

Deborah S. Kelley
School of Oceanography, University of Washington, Seattle, Washington 98195, USA

[1] The Atlantis Massif (Mid-Atlantic Ridge, 30°N) is an example of an oceanic core complex (OCC) exposed by a major fault system. Our integrated field and analytical study of mafic and ultramafic rocks exposed on the south wall of the massif demonstrates the complex interplay of fluids, mass transfer, and metamorphism in strain localization associated with the evolution of a major detachment shear zone and development of this OCC. Extensive talc-amphibole-chlorite metasomatism as well as heterogeneous, crystal-plastic to cataclastic deformation characterize a strongly foliated, 100-m-thick zone of detachment faulting. The metasomatic fault rocks are key elements of this OCC and record a deformation and metamorphic history that is distinct from the underlying basement rocks. Talc-rich fault rocks preserve textural and geochemical characteristics of their ultramafic protoliths. Although primary textures and mineral parageneses are commonly obliterated in rocks dominated by amphibole, bulk rock data point to a mafic protolith. Major and trace elements indicate a complex mutual interaction between gabbroic and ultramafic rocks during metasomatism, which together with microstructures suggest localized circulation of oxidizing, Si-Al-Ca-rich fluids and mass transfer in high strain deformation zones. This type of flow was distinct from the more pervasive circulation that led to strongly serpentinized domains in the south wall. In contrast, cataclastic microfracturing is associated with a dominantly static metasomatism in less deformed domains, suggesting that a significant amount of metasomatism was controlled by diffuse flow and mass transfer associated with fractures that lack a strong preferred orientation. Distinct differences in lithologies, metamorphic overprinting, and degree of deformation between the south wall and central dome of the Atlantis Massif demonstrate the complex lateral and vertical heterogeneity in composition, alteration, and structure of this OCC.

Components: 18,200 words, 12 figures, 5 tables.

Keywords: talc schist; serpentinite; oceanic core complex; detachment fault; hydrothermal processes; metasomatism.

Index Terms: 3015 Marine Geology and Geophysics: Heat flow (benthic); 3035 Marine Geology and Geophysics: Midocean ridge processes; 8135 Tectonophysics: Hydrothermal systems (0450, 1034, 3017, 3616, 4832, 8424); 8010 Structural Geology: Fractures and faults.

Received 14 July 2005; **Revised** 4 October 2005; **Accepted** 17 November 2005; **Published** 25 January 2006.

Boschi, C., G. L. Früh-Green, A. Delacour, J. A. Karson, and D. S. Kelley (2006), Mass transfer and fluid flow during detachment faulting and development of an oceanic core complex, Atlantis Massif (MAR 30°N), *Geochem. Geophys. Geosyst.*, *7*, Q01004, doi:10.1029/2005GC001074.

1. Introduction

[2] Oceanic core complexes (OCCs) are interpreted to be analogous to metamorphic core complexes in continental settings [e.g., *Crittenden et al.*, 1980; *Wernicke*, 1981] and are characteristically uplifted, dome-like massifs consisting of variably altered and deformed lower crustal and/or serpentinized upper mantle sequences, emplaced during periods of pronounced tectonic extension. Asymmetric detachment faulting and crustal accretion is particularly prevalent at the ends of slow-spreading ridge segments where it commonly leads to the formation of topographically high OCCs at inside corners of ridge-transform intersections. The formation of these domed massifs is generally attributed to a system of large-scale, low-angle normal (detachment) faults or shear zones and, in some cases such as in the MARK area and at the Atlantis Bank, Southwest Indian Ridge (SWIR), may be associated with varying degrees of magmatic accretion [e.g., *Karson and Dick*, 1983; *Karson*, 1990; *Dick et al.*, 1991; *Mutter and Karson*, 1992; *Tucholke et al.*, 1998; *Ranero and Reston*, 1999].

[3] A number of studies of the central Mid-Atlantic Ridge (MAR) indicate that OCCs feature extensive convex-up surfaces with spreading-direction-parallel corrugations and striations interpreted as the surface expressions of low-angle detachment faults [*Tucholke et al.*, 1998; *Cann et al.*, 1997; *Reston et al.*, 2002; *Blackman et al.*, 2004]. In many areas, direct observation and sampling of the detachment surfaces and associated fault rocks are hindered by the presence of rubble and sediments; however, recent studies of highly deformed rocks recovered from the striated surfaces of a peridotite massif near the Fifteen-Twenty Fracture Zone substantiates the interpretation that this surface represents a low-angle, detachment shear zone [*MacLeod et al.*, 2002; *Escartín et al.*, 2003].

[4] As in continental metamorphic core complexes, oceanic detachment faults expose a diverse suite of rock types that are derived from different lithospheric levels and which record varying magmatic/tectonic histories and conditions of metamorphism [e.g., *Gillis et al.*, 1993; *Kelley et al.*, 1993; *Karson and Lawrence*, 1997; *Karson*, 1998, 1999; *Taylor et al.*, 1999; *Dick et al.*, 2000; *Bach et al.*, 2004]. Some complexes record high-temperature deformation and metamorphism and may root in melt-rich zones in gabbroic crust (i.e., Atlantis Bank, SWIR, Site 735B) [*Dick et al.*, 1991, 2000]. Others, such as the MAR 15°45′N core complex, show localized deformation zones in relatively cold, serpentinized mantle peridotites with no evidence for significant high-temperature metamorphism and deformation [*MacLeod et al.*, 2002; *Escartín et al.*, 2003]. Although many of these studies have provided critical constraints on the formation of OCCs through detachment faulting, uncertainties remain as to the geometry and evolution of the faults within the lithosphere, the heterogeneity and distribution of lithologies exhumed in the footwall, the relationships between faulting and fluid flow, and the role of hydrothermal hydrous minerals in weakening the fault zones and facilitating prolonged slip. In this paper we combine geological, petrological, and microstructural observations with geochemical analyses of serpentinites, gabbros and metasomatically altered fault rocks collected by submersible and dredging at the Atlantis Massif (MAR, 30°N) [*Blackman et al.*, 1998, 2004; *Kelley et al.*, 2005]. Our studies provide additional constraints on the conditions of deformation, strain localization, and mass transport during a long-lived history of detachment faulting and exhumation of lower crustal and upper mantle sequences exposed in the OCC footwall along the southern wall of the massif.

2. Geological Overview and Sampling of the Atlantis Massif

[5] The Atlantis Massif (AM), located at 30°N at the inside corner of the eastern intersection of the Mid-Atlantic Ridge with the ~75 km, left-laterally slipping Atlantis Transform Fault (ATF), is a 1.5–2 my-old gabbro and peridotite massif that is interpreted as an oceanic core complex [*Cann et al.*, 1997; *Blackman et al.*, 1998, 2004]. This fault-bounded, dome-like massif is ~15–20 km across and is part of a 25-km-long, morphologically continuous ridge that defines the western side of the median valley of the MAR (Figure 1). This ridge is bounded to the west by a series of steep, west-facing scarps that are 15–20 km west of the median valley. To the south, the Atlantis Massif is truncated by a steep, deeply embayed and faulted escarpment with >3800 m of relief adjacent to the ATF valley [*Blackman et al.*, 2004]. The southern ridge has experienced significantly greater uplift than the central portion of the massif and shoals to ~730 m below sea level. The recently discovered Lost City Hydrothermal Field (LCHF) lies on a terrace at the top of this southern ridge and hosts numerous active and inactive carbonate-brucite

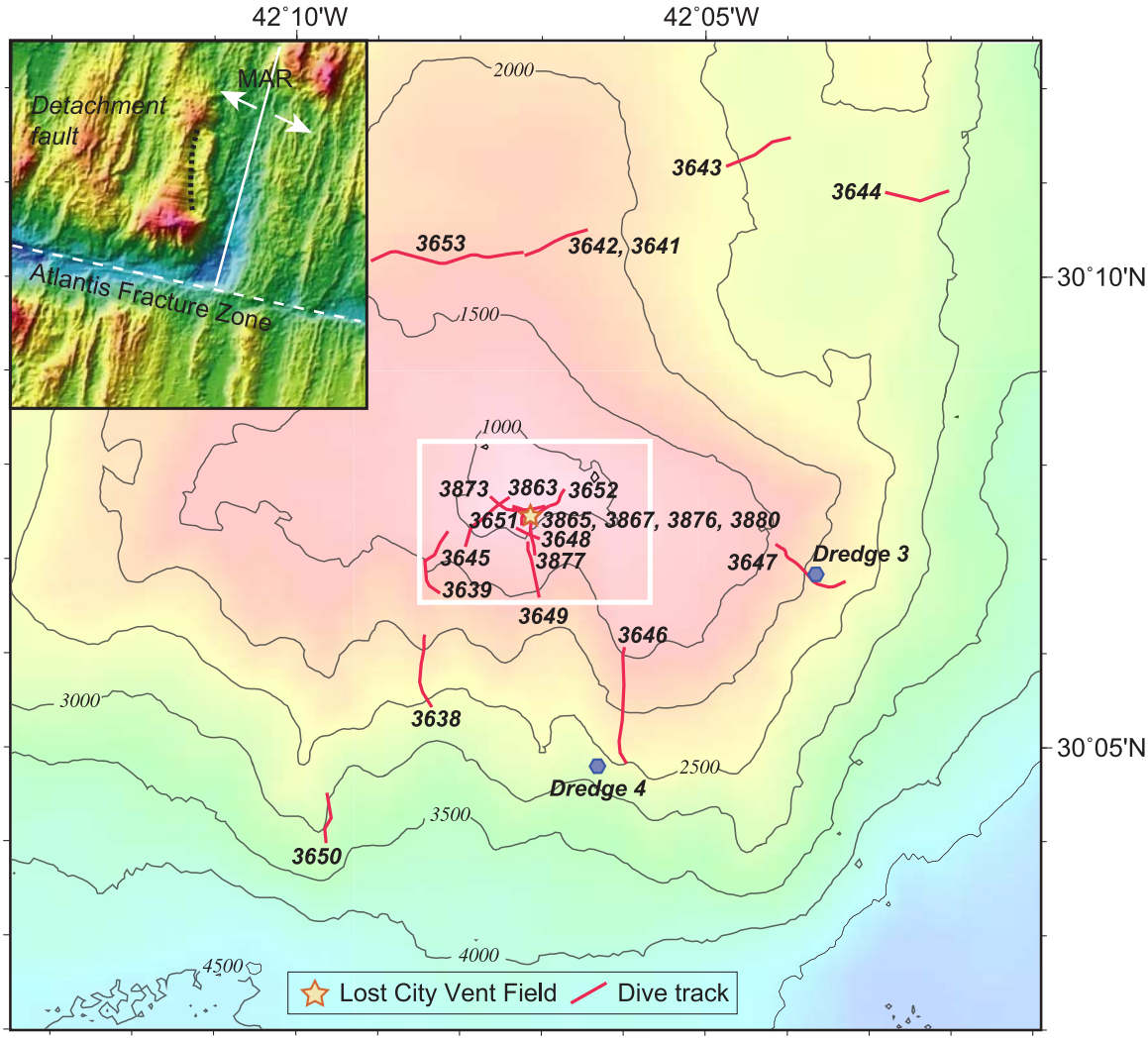

Figure 1. Location map of the study area of the Atlantis Massif and *Alvin* dives completed during the 2000 (MARVEL cruise; dives 3639 through 3652) and 2003 field campaigns (dives 3862 through 3881). Dense locations of *Alvin* dives around the Lost City Hydrothermal Field conducted in 2003 have been omitted for clarity. Inset shows location of the massif and local plate boundaries. White box shows area of sampling shown in detail in Figure 2.

chimneys that tower up to 60 m above the seafloor. The LCHF is the surface expression of warm (40–90°C), high pH (9–11) fluids emanating from fault zones that tap a region of active serpentinization in the underlying peridotites [*Kelley et al.*, 2001, 2005].

[6] Geological and geophysical investigations of the Atlantis Massif were conducted with the R/V *Atlantis* in 2000 (MARVEL cruise [*Blackman et al.*, 2004]). The area surrounding the LCHF was mapped and sampled in detail in 2003 [*Kelley et al.*, 2005], and further high-definition imagery and samples were obtained in 2005. These studies have shown that the dome-like massif is composed of variably altered and deformed harzburgites and gabbros with lesser basalts, capped by sedimentary rocks. Side-scan sonar data indicate that the top of the AM shows a distinct corrugated upper surface, which has been interpreted as a major detachment fault that was responsible for the widespread exposure of lower crustal and upper mantle rocks [*Cann et al.*, 1997; *Blackman et al.*, 2004]. Along the southern ridge, the corrugated surface extends eastward to the top of the median valley wall. Positive gravity anomalies [*Nooner et al.*, 2003; *Blackman et al.*, 2004] and high seismic velocities (8 km/s) at shallow depths (<1 km) below the seafloor [*Collins et al.*, 2001; *Canales et al.*, 2004] suggest that the interior of the massif is composed of weakly altered mantle peridotite and/or other olivine-rich lower crustal rocks.

Lower compressional velocities at shallow depths have been interpreted as evidence for the presence of an outer rind of serpentinite or other low-velocity material that is relatively thin (<~500 m) in the central part of the dome and somewhat thicker (~500–1000 m) along the southern wall. Multichannel seismic experiments over the Atlantis Massif identified major reflectors that are interpreted as an alteration front or as two distinct detachment faults that merge at depth with strongly serpentinized peridotite or other low-velocity material occurring between the faults [*Canales et al.*, 2004].

2.1. Southern Wall of the Atlantis Massif

[7] During the 2000 MARVEL cruise, considerable effort was made to document the detachment fault zone; however, a thin cover of lithified carbonate sediment and rubble on the top of the massif impeded detailed seafloor mapping and sampling of the fault surface [*Blackman et al.*, 2004; *Schroeder and John*, 2004]. Sampling of the central massif (*Alvin* dives 3641 to 3644, 3653) and in widely spaced transects over >4 km and at depths of 730 m to 3000 m along the southern wall (Figure 1, *Alvin* dives 3638 to 3641; 3645 to 3652) recovered variably altered and deformed serpentinites, gabbroic rocks, talc schists, sediments and minor basalts [see *Schroeder and John*, 2004, Table 1].

[8] Detailed mapping and sampling of the LCHF area and the detachment fault zone was carried out during a multidisciplinary field campaign on board the R/V *Atlantis* in April–May, 2003 (Cruise R/V *Atlantis* 7–34). The autonomous benthic explorer ABE was used to construct a high-resolution bathymetric map (gridded at 2 m) of the area; 19 dives with the submersible *Alvin* (*Alvin* dives 3862 through 3881) collected co-registered samples of vent fluids, vent material, sediments, basement rock, and macro-microfaunal samples [*Kelley et al.*, 2005]. *Alvin* dives 3863, 3865, 3867, and 3873 mapped and sampled in detail the detachment zone in nearly continuous cliff exposures along the scarps to the northwest and northeast of the LCHF; 47 samples were collected at depths between 750 and 880 m. Dive 3877 investigated the steep, N-S trending, fault-bounded, ridge below the LCHF field and recovered a further seven samples at depths of 900 to 1150 m (Figures 1 and 2). In the summer of 2005, further high-definition video imagery and sampling of the southern massif were carried out in the vicinity of the LCHF using the remotely operated vehicles (ROV) *Hercules* and *Argus* with the NOAA ship *Ronald H. Brown*. Preliminary results of this expedition, led by R. Ballard and D. Kelley, are available under http://oceanexplorer.noaa.gov/explorations/05lostcity/welcome.html and links therein. The 2005 field investigations substantiate the results presented here and provided further detailed three dimensional, meter-scale observations and imaging of the detachment zone and capping pelagic sediments over horizontal transects of ~4 km.

[9] Microstructural and mineral chemistry studies by *Schroeder and John* [2004] of samples collected during the MARVEL cruise provide an important basis for our investigations and established a history of metamorphism and deformation from granulite to greenschist-facies conditions during unroofing of the Atlantis Massif. On the basis of detailed analyses of nine samples from the immediate vicinity of the shear zone (<90 m structurally beneath the surface), *Schroeder and John* [2004] conclude that there is a ~10 m thick, brittle detachment fault at the top of the massif and that strain was localized by cataclasis and partitioned into altered peridotites by reaction softening in zones of extensive greenschist- and subgreenschist-facies metamorphism. In this paper, we present geochemical and petrological data of samples collected during the 2000 and 2003 cruises to reevaluate the tectonic and alteration history of the AM, in light of the more well-defined structural framework established in the follow up 2003 and 2005 cruises [*Kelley et al.*, 2005; J. A. Karson et al., Detachment Shear Zone on the Atlantis Massif Core Complex, Mid-Atlantic Ridge 30°N, submitted to *Geochemistry, Geophysics, Geosystems*, 2005 (hereinafter referred to as Karson et al., submitted manuscript, 2005)]. Our results differ from the earlier studies by *Schroeder and John* [2004] in that the detailed mapping and a higher density of sampling at the top of the southern wall of the massif allow us to document a mylonitic, low-angle detachment shear zone (DSZ), consisting of serpentinite and gabbroic rocks and marked by extensive metasomatism and high strain deformation. An overview of the geology of this detachment fault zone, based on integrated direct observations, photogeology and imaging, is given in a companion paper by Karson et al. (submitted manuscript, 2005) and provides the structural context for our study. Our results do not substantiate the presence of a narrow, brittle fault zone at the top of the massif nor the partitioning of strain into peridotites. Our field investigations and petro-

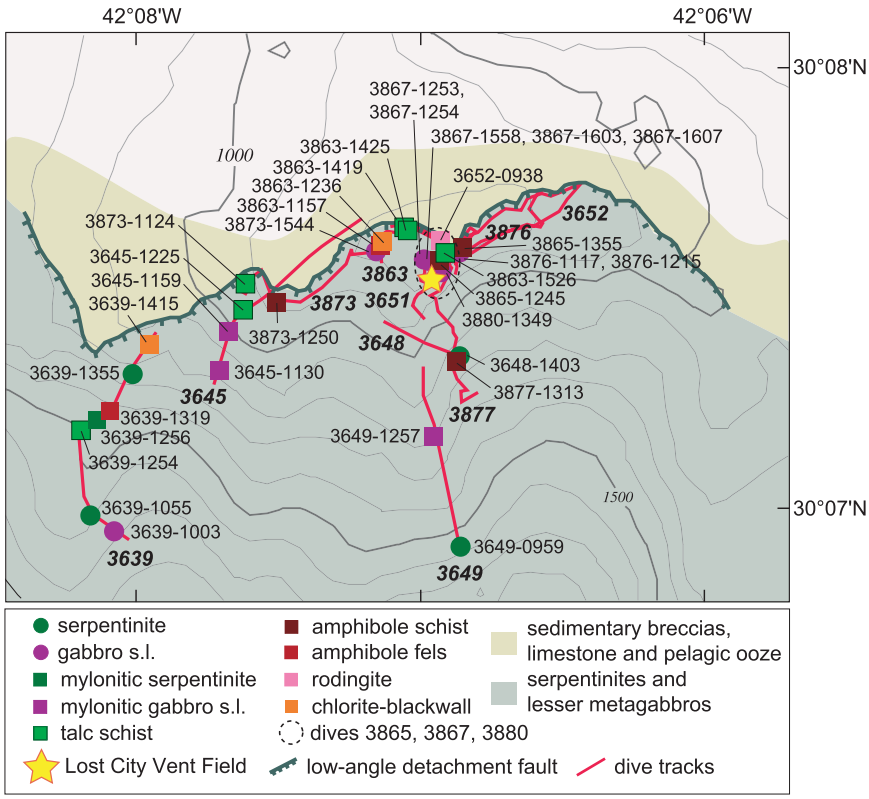

Figure 2. Simplified geologic map of the top of the south wall of the Atlantis Massif, showing the boundary of the detachment fault mapped in 2003 and with locations and corresponding lithologies of selected samples studied in this investigation.

logical and geochemical data indicate that pervasive talc-amphibole-chlorite metasomatism in the mafic and ultramafic rocks is a key element of the detachment fault zone in this portion of the OCC, and that the fault rocks record a heterogeneous, crystal-plastic to cataclastic deformation history that is distinct from the underlying basement rocks.

[10] The steep southern wall of the AM, which is the focus of our study, exposes a cross-section of the footwall of the OCC including the low-angle detachment shear zone and underlying basement rocks. Outcrop structures in the shear zone show variable anastomosing to planar fabrics (Figures 3a and 3b), with a persistent orientation, dipping <10–20° to the west or west-southwest. Sampling and high-definition imagery confirmed that foliated domains are predominantly mylonitic shear zones, consisting of strongly foliated serpentinites, metagabbroic rocks and talc-amphibole schists, surrounding lenses of less deformed material (Figure 3b). This foliated domain is interpreted as the detachment shear zone, which is about 100 m thick and can be traced continuously for at least 3 km in the tectonic transport direction (Karson et al., submitted manuscript, 2005). The highly foliated rocks and talc-amphibole schists grade downward into blocky, massive metagabbros and serpentinites that lack a strong outcrop-scale fabric. The main DSZ and underlying basement rocks are cut by discrete, anastomosing normal-slip, shear zones (Figure 3c) that are up to a few meters wide and consist of similar serpentinites and metasomatic talc- and amphibole bearing rocks (Karson et al., submitted manuscript, 2005).

[11] The strongly foliated rocks at the summit of the massif are overlain by laterally variable, consolidated rubble or sedimentary breccias that grade upward into variably indurated, bedded pelagic limestones and chalks (Figure 3d) [*Früh-Green et al.*, 2003; *Kelley et al.*, 2005; Karson et al., submitted manuscript, 2005]. The limestones and matrix of the breccias comprised well-preserved and abundant microfossils. The breccias contain poorly sorted, silt- to cobble-sized lithic fragments set in a well-lithified micritic carbonate matrix. The clasts show different degrees of deformation,

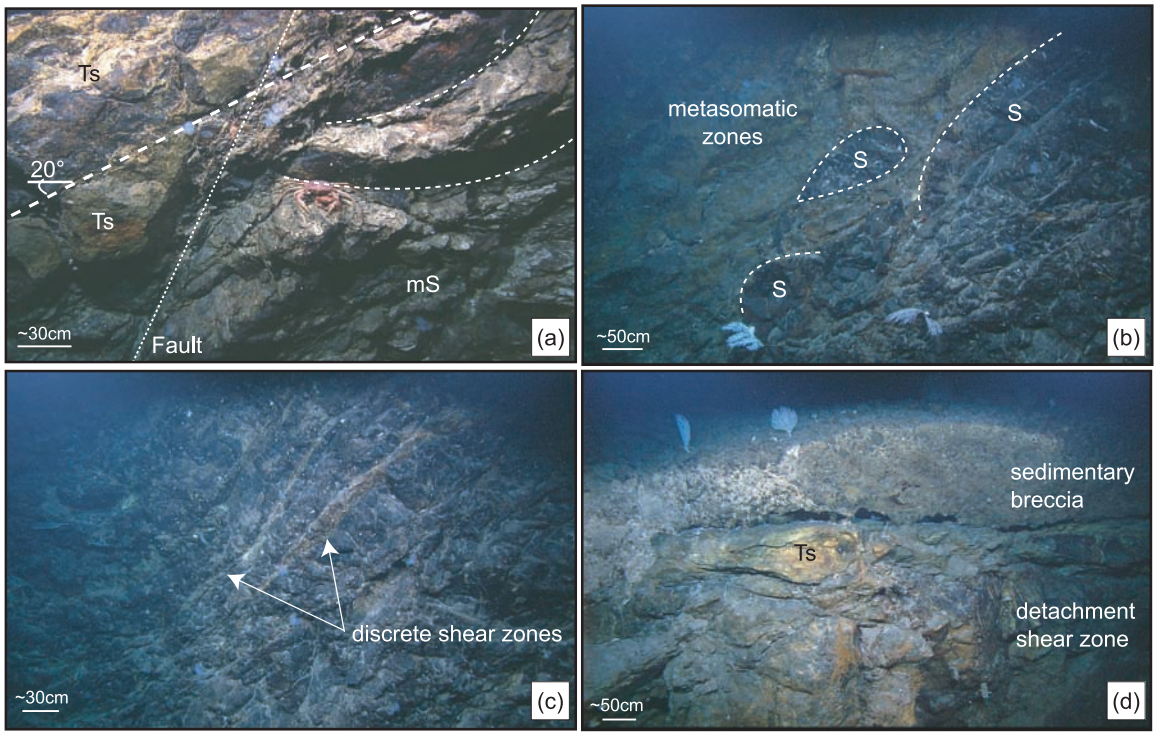

Figure 3. Examples of outcrops of the detachment shear zone (DSZ), looking north, near the top of the south wall of the Atlantis Massif, showing structural relationships between the variably deformed metasomatic talc-amphibole rocks (Ts), the mylonitic serpentinites (mS), and the less deformed serpentinites (S). Images were obtained from high-definition video with the ROV *Hercules* in vertical transects to the east of the LCHF. (a) Anastomosing fabrics in mylonitic serpentinites dipping about 20° west cut by a subvertical fault. (b) Planar to phaccoidal foliation dipping gently to the west-southwest and heterogeneous metasomatic zones with lens-shaped, less deformed serpentinites. (c) Discrete anastomosing mylonitic shear zones cutting the serpentinite foliation and containing metasomatic mineral assemblages. (d) Top of the AM south wall showing the DSZ overlain by sedimentary breccias with basaltic clasts. Lenses of light-colored metasomatic rocks (Ts) are clearly visible. Images courtesy of IFE, URI-IAO, UW, Lost City science party 2005, and NOAA.

alteration and veining, and are dominantly serpentinites, although a number of samples contain varying proportions of gabbroic and basaltic fragments. All phases of deformation and alteration observed in the basement rocks (discussed below) are recorded in lithic clasts found in the breccias. We interpret the sedimentary breccias as debris slide deposits shed onto the detachment fault surface (Karson et al., submitted manuscript, 2005) after the main phases of serpentinization, metasomatism and detachment faulting. Detachment faulting led to the initial exposure of the peridotites and may have provided important fluid pathways during the early evolution of the massif. Fracturing, mass wasting, carbonate precipitation, and active venting at the LCHF are currently controlled by steeply dipping normal faults that offset the basement rocks and postdate detachment faulting [*Früh-Green et al.*, 2003; *Kelley et al.*, 2005; Karson et al., submitted manuscript, 2005]. These normal faults, striking parallel to the regional trend of the ATF or parallel to the MAR, are the latest deformation structures and have probably developed in response to the uplift of the massif.

2.2. Drilling in the Central Atlantis Massif

[12] The central Atlantis Massif was the target of two legs of the Integrated Ocean Drilling Program (IODP Expeditions 304 and 305) in 2004/2005 to continuously drill and sample this OCC and its capping detachment fault system [*Expedition Scientific Party*, 2005a, 2005b]. Drilling at IODP Hole U1309D, on the crest of the central dome of the massif at a depth of 1656 meters below the surface (mbsf), recovered a 1.4 km suite of dominantly gabbroic rocks (~91% of the total recovery) with intercalated ultramafic rocks (6%).

The recovered lithologies range from dunitic troctolite, troctolite, olivine gabbro, gabbro and gabbronorite to evolved oxide gabbro, and are among the most primitive rocks collected along the MAR [*Expedition Scientific Party*, 2005b]. Tholeiitic diabase and basalt were recovered only in the upper 130 m of the footwall, and minor occurrences of serpentinites were found in the upper 400 m (0.3% of the total recovery). Preliminary results show that the alteration assemblages record cooling of the gabbroic rocks from magmatic to zeolite-facies conditions, with a dominance of low-temperature (<500°C) overprinting and a notable lack of extensive amphibolite-facies alteration and deformation [*Expedition Scientific Party*, 2005a, 2005b]. Sampling of the hanging wall rocks and the upper 20 m of the footwall that was believed to be the region of detachment faulting, proved to be difficult.

[13] The dominance of primitive gabbroic rocks and absence of significant amounts of serpentinized mantle peridotites and talc schists at IODP Site U1309 contrasts greatly with our studies of the southern wall of the massif, 5 km to the south, and is inconsistent with predictions of a predominance of upper mantle sequences based on previous interpretations of seismic refraction data centered ~2 km north of Hole U1309D [*Collins et al.*, 2001; *Canales et al.*, 2004; *Expedition Scientific Party*, 2005b]. The contrasting results reflect differences in sampling techniques and position within the OCC, and highlight the highly heterogeneous nature of the Atlantis Massif: drilling at IODP Hole 1309D provided nearly continuous sampling of variations in composition, metamorphism and deformation in a one dimensional core of the central massif; whereas our submersible field investigations provided intermittent, targeted sampling on a broader, three dimensional outcrop scale of the southern wall that has presently been uplifted to water depths of ~730 m. Despite differences in approaches, these studies clearly show that the two areas are distinctly different and that there must be major structural and compositional variations on a scale of a few kilometers from N to S across the Atlantis Massif. The data and interpretations presented here focus on the highly uplifted, southern portion of the massif.

3. Analytical Methods

[14] Detailed petrographic examination of >150 gabbroic and peridotite samples collected from the shear zone and surrounding areas document a remarkable range of microstructures and textural relationships that record the tectonic evolution of the AM. With the exception of sample 3642-1309, all samples discussed here were recovered from the southern wall of the massif. It is important to note that fresh samples were difficult to obtain with *Alvin*, and thus our samples are biased toward more fractured, altered and weathered rock types. Petrographic observations (optical microscopy and scanning electron microscopy with EDS capabilities) of thin sections were used to establish textural relationships, to determine mineral phases and to identify relict minerals of the original protoliths. X-ray diffraction (XRD) spectra were acquired on bulk rock powders and veins with a computer-aided, Scintag X-ray diffractometer using CuKa radiation at 45 kV and 40 mÅ. Data were recorded between 4° and 70° 2θ with steps of 0.02° 2θ and one second counting per step.

[15] Quantitative mineral chemistries (Tables 1 and 2) were determined at the Institute for Mineralogy and Petrology (ETH-Zurich) and at the Centro di Studio per la Minerogenesi e Geochimica Applicata (C.N.R., Florence). Measurements made at the C.N.R. Florence were carried out on a JEOL JXA-8600 electron microprobe coupled with four wavelength dispersive (WDS) spectrometers, each with two flipping analyzing crystals for quantitative analyses and an energy dispersive spectrometer (EDS) for qualitative analyses. The operating conditions were 15 kV accelerating potential, 10 nA current, and 2–5 μm beam size. At the ETH-Zurich, mineral chemistries were determined using a JEOL JXA-8200 electron microprobe with five WDS spectrometers, each with two flipping analyzing crystals for quantitative analyses and EDS for qualitative analyses. The operating conditions were 15 kV accelerating potential, 20 nA current, and 1–10 μm beam size.

[16] Major-element analyses and trace elements of whole rock samples were performed by inductively coupled plasma-mass spectrometry (ICP-MS) at two commercial research laboratories: at the Activation Laboratories Ltd. (Ancaster, Canada) using its research quality fusion-ICP method and inductively ICP-MS respectively; and at CRPG-Nancy (France) by ICP-AES and ICP-MS after fusion with $LiBO_2$ and dissolution by HNO_3. Crossed-check analyses were performed to guarantee analytical consistency. Determination of CO_2 contents was performed at the ETH-Zurich by coulometric titration (Coulometer UIC CM5012), with

an analytical precision of ±0.1 weight%. Density measurements of whole rocks were performed by helium pycnometer (AccuPyc 1330) at the Geological Institute of the ETH-Zürich. True densities are measured using helium gas since it penetrates surface flaws down to about one Angstrom, thereby enabling the measurement of rock powder volumes with great accuracy.

[17] Here we present detailed geochemical analyses of representative samples of the metasomatic rocks and compare these with variations in compositions of the serpentinite and gabbroic rocks (Tables 3 through 5) from the detachment shear zone near the top of the Atlantis Massif. In a companion paper (C. Boschi et al., manuscript in preparation, 2005), we present petrological studies, mineral chemistry, and bulk rock geochemical data on the underlying, non-sheared basement serpentinites to evaluate chemical changes and mass balance during long-lived serpentinization of the less deformation basement in the south wall of the Atlantis Massif.

4. Results

[18] Our detailed field investigations and the recovery of fault rocks and the underlying basement rocks provide an important opportunity to document the heterogeneity and distribution of lithologies exhumed in the footwall of the Atlantis Massif and to examine the relationships between deformation, fluid flow, and mass transfer during long-lived detachment faulting. In the following subsections, we present detailed petrological and bulk rock geochemical data on the gabbroic rocks, the serpentinites and the metasomatic rocks from the southern-most portion of the Atlantis Massif. Integration of these data allows us to unravel a complex history of deformation, strain localization, hydrothermal alteration, and metasomatism during the evolution of this oceanic core complex. Comparison of our studies with preliminary results of drilling by IODP provides important constraints on the major structural and compositional variations on a scale of a few kilometers from N to S across the Atlantis Massif.

4.1. Petrography and Mineral Chemistry

[19] Our current seafloor mapping and sampling of the southern wall of the Atlantis Massif indicates that variably serpentinized peridotite is the dominant rock type, comprising ~60% of the recovered basement samples (Figure 2). The serpentinites are associated with a heterogeneous suite of gabbroic rocks, all of which display diverse magmatic histories and highly variable degrees of alteration and deformation (Figures 4 through 7). The two rock-types are difficult to distinguish in seafloor outcrops; however, no extensive outcrops of gabbro could be identified along the southern wall during any of our field campaigns. Samples of variably altered serpentinites were consistently recovered from outcrops that showed varying degrees of foliation or had a knobby to massive appearance, and samples of gabbroic rocks were invariably collected in close vicinity to samples of serpentinites. The lack of extensive gabbro outcrops together with the heterogeneous mineralogies and the distribution of gabbroic rocks recovered along the southern wall suggests that they may occur as smaller magmatic bodies or lenses in a peridotite-dominated upper mantle section of the lithosphere. This heterogeneity and distribution further brings to light the distinct differences in lithologies and crustal composition between the southern wall of the AM and the central dome region sampled during IODP Expeditions 304 and 305 [*Expedition Scientific Party*, 2005a, 2005b].

[20] Basaltic rocks were recovered mainly from the surface of the dome and occur as variably rounded blocks of rubble in the sedimentary breccias or as isolated blocks in the pelagic carbonate sediments (Figure 3d). In many samples of the sedimentary breccias, basaltic clasts are the dominant lithic component. The origins of the basaltic clasts and the sedimentary breccias that overlie the foliated serpentinite basement rocks are enigmatic because the top of the massif presently lacks significant relief. This suggests that they represent fractured, basalt-dominated hanging wall material that was deposited as debris flows over the detachment surface when it defined the eastern flank of the massif (Karson et al., submitted manuscript, 2005). The presence of variably altered and metasomatic peridotite and gabbroic components in the breccias also suggests that the detachment fault zone is located close to the serpentine/basalt interface and that this zone must have been exposed, locally eroded, and deposited as lithic fragments in the overlying cap rock sediments.

[21] Deformation recorded in the basement rocks increases dramatically in the upper 100 m of the scarp. The DSZ is marked by intensely deformed serpentinites, talc-amphibole schists, and lesser metagabbroic rocks in variably foliated, lensoid

domains separated by more continuous anastomosing shear zones (Figure 3c) (Karson et al., submitted manuscript, 2005). Relatively weakly deformed, massive lithologies and minor veining pass upward into areas of highly strained material with cataclastic to mylonitic shear zones spaced at intervals of centimeters to decimeters. The massive ultramafic rocks lack a strong outcrop-scale fabric, but samples preserve typical mantle crystal-plastic deformation fabrics, particularly evident by porphyroclastic orthopyroxene textures and holly leaf spinel grains. Petrological and geochemical analyses of the AM basement rocks, presented below and in Figures 4 through 7, indicate a heterogeneous and complex history of deformation and hydrothermal circulation.

4.1.1. Gabbroic Rocks

[22] The heterogeneous suite of gabbroic and related rocks recovered by submersible and dredging at the Atlantis Massif are dominantly medium- to coarse-grained gabbros with lesser occurrences of gabbronorite, olivine-bearing gabbro, Fe-Ti oxide–bearing gabbronorite, pyroxenite, microgabbro, and diabase dikes. We found no samples that could unequivocally be identified as troctolitic in compositions, in contrast to the relative abundance of troctolites (2.7%) and olivine gabbro/troctolitic gabbro (25.5%) recovered by IODP [*Expedition Scientific Party*, 2005a, 2005b]. The gabbros *s.s.* commonly have granular textures and are dominated by primary clinopyroxene and plagioclase with minor amounts of oxide minerals, orthopyroxene and olivine. Plagioclase typically shows undulatory extinction and has locally undergone minor subgrain development and recrystallization. *Schroeder and John* [2004] interpret the grain boundaries between plagioclase neoblasts and plagioclase porphyroclasts as evidence for greenschist-facies, grain-boundary migration and recrystallization. Clinopyroxene occurs as primocrysts or as interstitial phases, which are easily distinguished on the basis of texture. The primocrysts are predominantly millimeter-sized and show a granular, euhedral to subhedral habit. Late-stage pyroxenes (<1 mm in size) are anhedral with irregular, curved grain boundaries, and in general show no exsolution lamellae. Late stage pyroxenes typically rim clinopyroxene primocrysts, or grow on the boundaries between the primary mafic silicate phases. The late-stage pyroxenes are associated with secondary, interstitial, brownish amphiboles. Secondary amphiboles with different textures and compositions are ubiquitous and occur together with chlorite and secondary oxides; albite and quartz are locally observed.

[23] Despite an overall chemical homogeneity (Figure 8; Table 3), the metamorphosed gabbros *s.s.* display highly variable textures. They have experienced two main stages of retrograde metamorphism. An early phase of post-magmatic, high-temperature metamorphism [*Schroeder and John*, 2004] is characterized by dynamic recrystallization of plagioclase and by secondary brownish acicular to granular hornblende that replace primary igneous pyroxene or pyroxene plus plagioclase along grain boundaries (interstitial hornblende). This first phase of alteration under amphibolite- to granulite-facies conditions [*Schroeder and John*, 2004] is associated with crystal-plastic deformation, represented by microstructures and textures ranging from bent plagioclase with polysynthetic twinning to strongly banded amphibolites composed of foliated secondary amphiboles with bands of secondary plagioclase (e.g., sample 3649-1257). High-strain deformation resulting in protomylonitic to ultramylonitic shear zones in a few gabbro blocks was also observed (e.g., samples 3645-1130 and 3649-1257).

[24] A second phase of alteration is marked by lower temperature (<~500°C) mineral assemblages consisting predominantly of tremolitic to actinolitic, greenish amphibole and dark blue chlorite [*Schroeder and John*, 2004]. The new hydrothermal minerals form in vein-like zones, as reaction rims along pyroxene/plagioclase contacts, or as pseudomorphs after pyroxenes/amphibole. Our petrographic studies indicate that cataclastic deformation in the gabbros is dominated by microfractures to millimeter-wide fractures and veins that are filled with greenschist-facies mineral assemblages.

[25] Formation of the early amphibolite-facies mineral assemblages is likely related to a near-axis, high-temperature phase (>~600°C) of seawater penetration and hydrothermal alteration, as is characteristic of slow-spreading mid-ocean ridge environments [e.g., *Gillis et al.*, 1993; *Kelley et al.*, 1993]. The presence of high-temperature mylonitic deformation in the gabbroic rocks suggests that detachment faulting may have been initiated very early in the metamorphic/tectonic evolution of this portion of the ridge axis [see also *Schroeder and John*, 2004]. The second phase of alteration and deformation was likely related to unroofing. These episodes of metamorphism have resulted in heterogeneous alteration and mixed disequilibrium

assemblages containing high-temperature igneous or post-magmatic minerals overprinted by lower temperature metamorphic mineral assemblages. The retrograde metamorphism is associated with mixed crystal-plastic and cataclastic deformation at amphibolite- to greenschist-facies conditions.

[26] The Fe-Ti oxide-bearing gabbros recovered at the AM are defined by the occurrence of more than 2% modal primary Fe-Ti-oxide minerals. These occur as interstitial anhedral grains and are also found between deformed and recrystallized plagioclase. Some of the oxide gabbros contain apatite and zircon as accessory minerals. The textural relationships between deformed plagioclase and oxides are similar to those described from gabbroic samples recovered in ODP Holes 1270B [*Kelemen et al.*, 2004] and 735B [e.g., *Dick et al.*, 2000]. Secondary Fe-Ti oxides in a few deformed samples (e.g., sample 3647-1323) occur as exsolution products of clinopyroxenes and are commonly dispersed in brown and green amphibole rims where clinopyroxene has been hydrothermally altered. Sample 3649-1257 contains interstitial elongated Fe-Ti oxides that are concordant with the foliation.

[27] Samples 3650-1437, 3652-0938, 3867-1253 and 3867-1254 have undergone varying degrees of rodingitization. Rodingite forms through calcium enrichment and desilicification of mafic rocks adjacent to or within serpentinites [*O'Hanley*, 1996]. In ophiolite terrains, rodingites typically consist of varying proportions of epidote-group minerals, Ca-rich garnet (grossular, hydrogrossular, andradite), diopside, tremolite, chlorite, prehnite, vesuvianite, margarite, and other Ca-Al silicates. Protoliths rich in Fe and Mg and poor in alkalis, such as gabbros and basalts, may retain remnants of their original mineral assemblages, such as augite (or other clinopyroxenes) and rarely plagioclase. These rocks commonly have prehnite or epidote-group minerals as early phases of rodingitization [*O'Hanley*, 1996].

[28] Macroscopically, the rodingite sample 3650-1437 (Figure 5e) is as a dense white and pink rock surrounding small darker remnants of the coarse-grained protolith. In thin section, the darker domains consist of green actinolitic amphibole that presumably replaced primary clinopyroxene. During alteration to amphibole, the primary mafic crystals underwent topotactic replacement and subgrain development. The rodingite mineral assemblage is dominated by both coarse- and fine-grained prehnite (comprising white zones in hand sample) associated with very fine-grained aggregates of prismatic clinozoisite with minor titanite and chlorite (concentrated in pink zones in hand sample). Prehnite forms faintly yellowish-white lamellar to platy aggregates, some of the plates occur as fan-shaped arrays (Figure 7e). Fine-grained aggregates of clinozoisite appear as cloudy darker areas. The presence of clinozoisite and prehnite are confirmed by XRD analyses. Small pockets of bluish chlorite are observed together with minor crystals of titanite. Sample 3652-0938 (Figure 5f) shows similar minerals characteristic of rodingitization but contains relics of fine-grained recrystallized plagioclase together with a brownish amphibole rimmed by greenish amphibole. The latter appears to have grown contemporaneous with the prehnite and clinozoisite. Samples 3867-1253 and 3867-1254 show incipient rodingitization: these are foliated metagabbros intruded by thick prehnite veins, with minor zeolite and hydrogarnet, that show a fan-shaped crystal habit and high birefringence in thin section (Figure 7e).

[29] *Alvin* dive 3647, on the south-east shoulder of the AM (Figure 1), was made on an extensive talus slope and recovered an unusual series of mafic and ultramafic rocks that include serpentinite, talc- and amphibole-rich fault rocks and texturally complex metagabbros and metabasalts. This suite of samples shows evidence of magmatic mixing, melt impregnation and ultramafic-mafic interaction and has distinctive geochemical compositions (discussed below).

4.1.2. Serpentinite and Serpentinized Peridotite

[30] The ultramafic rocks recovered along the south wall of the AM are spinel harzburgites in composition with medium- to coarse-grained porphyroclastic textures [*Mercier and Nicolas*, 1975]. Primary assemblages consist of olivine, orthopyroxene, and chromium spinel with rare clinopyroxene. All samples recovered in our studies are extensively serpentinized and are affected by at least 70% to 100% replacement of the primary minerals [*Boschi et al.*, 2003]. However, observations during the *Alvin* dives and from high-definition seafloor imagery indicated that the steep exposures along the southern wall of the AM consist predominantly of massive outcrops that we believe represent less sheared and altered mantle peridotites (Karson et al., submitted manuscript, 2005).

[31] Serpentinization to lizardite ± chrysotile and magnetite is characterized by the formation of

Table 1. Selected Electron Microprobe Analyses of Secondary Amphiboles in Metasomatic Rocks at the South Wall of the Atlantis Massif[a]

Sample	3647-1359							3646-1205					3646-1000		3646-1409		D4-9	
Analysis No.	1	2	3	4	5	6	7	1	2	3	4	5	1	2	1	2	1	2
Mineralogy	Anth/Cum	Anth/Cum	Anth/Cum	Act	Act	Fe-Act	Act Hbl	Mg-Hbl	Ed	Ed	Act	Trem	Ed	Trem	Ed	Ed	Trem	Ed
SiO_2	57.85	56.93	57.60	56.53	57.38	53.29	53.25	49.00	47.93	47.43	55.06	56.44	49.75	58.94	48.45	48.13	57.31	51.48
TiO_2	0.13	0.29	0.25	0.07	0.10	0.26	1.00	1.61	2.93	2.18	0.18	<d.l.	0.03	<d.l.	0.23	0.27	0.08	0.15
Cr_2O_3	0.14	0.21	0.12	0.14	0.16	0.11	0.80	0.89	0.08	0.26	0.05	0.16	1.00	0.06	0.65	0.72	0.20	0.53
Al_2O_3	0.52	1.07	0.87	0.41	0.57	0.41	3.50	7.59	7.30	8.22	1.86	0.20	9.01	0.18	9.42	9.67	2.08	7.12
FeO	10.13	9.94	9.45	9.00	4.58	20.79	4.49	5.78	6.20	6.16	7.94	2.64	1.25	1.03	4.30	4.21	1.99	2.49
MnO	0.21	0.22	0.18	0.33	0.13	0.49	0.11	0.12	0.10	0.11	0.06	0.11	0.07	0.07	0.11	0.09	0.07	0.06
NiO	0.14	0.18	0.20	0.07	0.07	0.07	0.20	0.17	0.18	0.18	0.06	0.12	0.10	0.07	0.15	0.17	0.06	0.11
MgO	27.21	26.79	27.49	18.91	22.58	11.13	21.05	19.37	18.99	19.16	19.44	25.30	21.37	24.60	20.19	20.01	23.06	21.45
CaO	1.21	1.71	1.59	12.14	11.91	10.60	11.53	11.44	11.17	11.29	13.24	12.04	12.33	13.09	11.53	11.62	12.56	12.55
Na_2O	0.17	0.40	0.32	0.40	0.44	0.72	1.11	1.54	2.51	2.14	0.32	0.02	1.77	0.06	2.54	2.52	0.39	1.89
K_2O	0.01	0.02	<d.l.	<d.l.	0.02	0.02	0.12	0.11	0.18	0.16	0.01	<d.l.	0.21	0.02	0.16	0.12	<d.l.	<d.l.
Cl	0.01	0.02	0.02	0.01	0.01	0.01	0.02	0.04	0.02	0.02	<d.l.	<d.l.	0.10	<d.l.	0.03	0.03	<d.l.	<d.l.
F	<d.l.	<d.l.	0.05	<d.l.	0.02	0.02	0.03	0.04	0.04	0.12	0.01	<d.l.	-	-	-	-	-	-
Total	97.71	97.75	98.07	97.99	97.94	97.89	97.17	97.61	97.55	97.30	98.22	97.03	96.89	98.12	97.73	97.53	97.80	97.83
Si	7.94	7.84	7.87	7.98	7.92	8.01	7.50	6.93	6.88	6.78	7.70	7.71	6.95	7.97	6.82	6.79	7.85	7.15
Al^{IV}	0.06	0.16	0.13	0.02	0.08		0.50	1.07	1.12	1.22	0.30	0.03	1.05	0.03	1.18	1.21	0.15	0.85
Al^{VI}	0.02	0.01	0.01	0.05	0.01	0.07	0.08	0.20	0.12	0.16	0.00		0.43	0.00	0.39	0.40	0.18	0.31
Ti	0.01	0.03	0.03	0.01	0.01	0.03	0.11	0.17	0.32	0.23	0.02		0.00		0.02	0.03	0.01	0.02
Cr	0.02	0.02	0.01	0.02	0.02	0.01	0.09	0.10	0.01	0.03	0.01	0.02	0.11	0.01	0.07	0.08	0.02	0.06
Fe^{3+}											0.17	0.53						
Fe^{2+}	1.16	1.14	1.08	1.06	0.53	2.61	0.53	0.68	0.74	0.74	0.76		0.15	0.12	0.51	0.50	0.23	0.29
Mg	5.57	5.50	5.60	3.98	4.65	2.49	4.42	4.08	4.06	4.08	4.05	5.15	4.45	4.96	4.24	4.21	4.70	4.44
Mn	0.02	0.03	0.02	0.04	0.02	0.06	0.01	0.01	0.01	0.01	0.01	0.01	0.01	0.01	0.01	0.01	0.01	0.01
Ni	0.02	0.02	0.02	0.01	0.01	0.01	0.02	0.02	0.02	0.02	0.01	0.01	0.01	0.01	0.02	0.02	0.01	0.01
Ca	0.18	0.25	0.23	1.84	1.76	1.71	1.74	1.73	1.72	1.73	1.98	1.76	1.84	1.90	1.74	1.76	1.84	1.87
Na	0.05	0.11	0.08	0.11	0.12	0.21	0.30	0.42	0.70	0.59	0.09	0.00	0.48	0.02	0.69	0.69	0.10	0.51
K	0.00	0.00				0.00	0.02	0.02	0.03	0.03	0.00	0.00	0.04	0.00	0.03	0.02		
Total	15.05	15.11	15.08	15.11	15.12	15.21	15.32	15.44	15.73	15.62	15.09	15.00	15.52	15.02	15.72	15.71	15.10	15.51
H	2.00	2.00	1.97	2.00	1.99	1.99	1.98	1.97	1.98	1.94	2.00	2.00	1.98	2.00	1.99	1.99	2.00	2.00
Cl	0.00	0.00	0.00	0.00	0.00	0.00	0.01	0.01	0.00	0.00			0.02		0.01	0.01		
F			0.02		0.01	0.01	0.01	0.02	0.02	0.05	0.00							
NaK(A)	0.05	0.11	0.08	0.11	0.12	0.21	0.32	0.44	0.73	0.62	0.09	0.00	0.52	0.02	0.72	0.71	0.10	0.51
X_{Mg}	0.83	0.83	0.84	0.79	0.90	0.49	0.89	0.86	0.85	0.85	0.84	1.05	0.97	0.98	0.89	0.89	0.95	0.94

[a] Notes: <d.l., below detection limit; "-", not determined; Trem, tremolite; Act, actinolite; Anth/Cum, Anthophyllite/Cummingtonite; Fe-Act, ferro-actinolite; Act-Hbl, actinolitic hornblende; Mg-Hbl, magnesio-hornblende; Ed, edenite. Structural formula are based on 23O and 2(OH, F, Cl) [*Leake*, 1978].

Table 2. Selected Chemical Compositions of Chlorites in Metasomatic Rocks at the South Wall of the Atlantis Massif[a]

Sample	D4-4	3647-1359	3863-1236		3646-1205		D4-9			
Analysis		1	1	2	1	2	1	2	3	4
Mineralogy	1	talc-chl	clinochl	clinochl	clinochl	talc-chl	penn	talc-chl	talc-chl	talc-chl
SiO_2	28.71	38.21	29.60	30.25	31.33	40.29	34.64	41.50	40.64	41.13
TiO_2	<d.l.	0.01	0.04	0.04	0.03	0.02	0.07	<d.l.	0.03	0.04
Cr2O3	2.56	0.16	0.04	<d.l.	0.14	1.36	0.03	0.06	0.02	<d.l.
Al_2O_3	17.13	10.07	20.55	18.40	15.55	7.81	12.10	6.38	2.74	2.32
FeO	14.62	7.70	6.77	7.85	9.76	9.28	4.60	4.73	4.87	4.67
MnO	<d.l.	0.10	0.02	0.04	0.14	0.22	0.04	0.11	0.18	0.14
NiO	0.43	0.17	0.14	0.16	0.14	0.22	0.14	0.08	0.06	0.07
MgO	24.06	30.22	30.21	29.62	29.89	27.85	35.71	34.67	38.23	38.83
CaO	0.08	0.17	0.01	0.05	0.02	0.14	<d.l.	0.01	0.04	0.02
Na_2O	0.07	0.05	0.03	0.02	<d.l.	0.01	0.04	0.07	<d.l.	<d.l.
K_2O	<d.l.	0.02	0.01	0.01	0.01	0.03	0.12	0.04	<d.l.	<d.l.
Cl	0.02	0.01	0.01	<d.l.	<d.l.	0.02	<d.l.	<d.l.	0.03	0.03
F	<d.l.	0.01	<d.l.	<d.l.	<d.l.	0.04	<d.l.	<d.l.	0.06	0.03
Total	87.65	86.87	87.42	86.45	87.01	87.22	87.49	87.63	86.80	87.22
Si	5.764	7.247	5.650	5.88	6.103	7.627	6.515	7.672	7.697	7.747
Al^{IV}	2.236	0.753	2.350	2.12	1.897	0.373	1.485	0.328	0.303	0.253
Al^{VI}	1.817	1.498	2.273	2.09	1.674	1.369	1.197	1.062	0.309	0.262
Ti		0.001	0.006	0.01	0.004	0.003	0.010		0.004	0.005
Cr	0.406	0.024	0.006		0.021	0.204	0.004	0.008	0.003	
Fe^{3+}		0.445				0.720		0.419	0.041	0.034
Fe^{2+}	2.464	0.776	1.106	1.29	1.666	0.749	0.839	0.312	0.730	0.702
Mn	0.000	0.017	0.004	0.01	0.023	0.035	0.007	0.017	0.029	0.023
Mg	7.200	8.544	8.595	8.58	8.680	7.859	10.011	9.554	10.794	10.903
Ni	0.069	0.025	0.021	0.03	0.023	0.033	0.021	0.011	0.009	0.011
Ca	0.017	0.034	0.002	0.01	0.003	0.028		0.001	0.007	0.005
Na	0.054	0.035	0.022	0.02		0.007	0.028	0.050	0.001	
K		0.009	0.005		0.005	0.013	0.059	0.017	0.002	
Cl	0.011	0.005	0.006			0.010			0.017	0.019
F		0.008	0.000			0.047			0.069	0.041
Total	36.03	35.41	36.04	36.02	36.10	35.02	36.18	35.45	35.93	35.94
OH	15.99	15.99	15.99	16.00	16.00	15.94	16.00	16.00	15.91	15.94
Fe/Fe+Mg	0.25	0.13	0.11	0.13	0.16	0.16	0.08	0.07	0.07	0.06

[a] Notes: <d.l., below detection limit; structural formulas are based on 36 (O, OH) [*Bailey*, 1980]. Clinochl, clinochlore; Penn, penninite (Al-rich clinochlore); Talc-chl, talc-chlorite. Chlorite commonly occurs as sub-millimeter sized intergrowths with talc (denoted as talc-chlorite analyses).

pseudomorphic ribbon or mesh serpentine textures after olivine [*Wick and Whittaker*, 1977]. Orthopyroxene is altered to bastite or to fibrous talc ± chlorite; magnetite is abundant in some samples and tends to concentrate along mesh rims and within serpentinite veins. Pervasive alteration is associated with multiple generations of microscopic to mesoscopic veins consisting of varying proportions of serpentine, magnetite and chlorite.

[32] Most of the peridotite samples preserve remnants of porphyroclastic fabrics typical of oceanic mantle peridotites [*Mercier and Nicolas*, 1975], but in contrast to the gabbroic rocks, show little or ambiguous evidence of crystal-plastic deformation and a high-temperature phase of hydrous metamorphism that might be associated with early detachment faulting. Early deformation, presumably related to the initial stages of unroofing of the AM, is marked by undulose extinction and bent cleavage of pyroxene pseudomorphs and in a few mylonitic samples, by narrow bands of recrystallized olivine. The predominance of ribbon serpentine textures in the serpentinites could also reflect a pre-existing foliation and the presence of bands of recrystallized olivine formed during crystal-plastic deformation. Sample D4-3 is a rare example of a high-temperature ultramafic mylonite characterized by a core of serpentinite rimmed by mylonitic harzburgite. Cataclastic deformation, in the form of microfractures to millimeter-wide fracture-fillings, is widespread and is associated with the

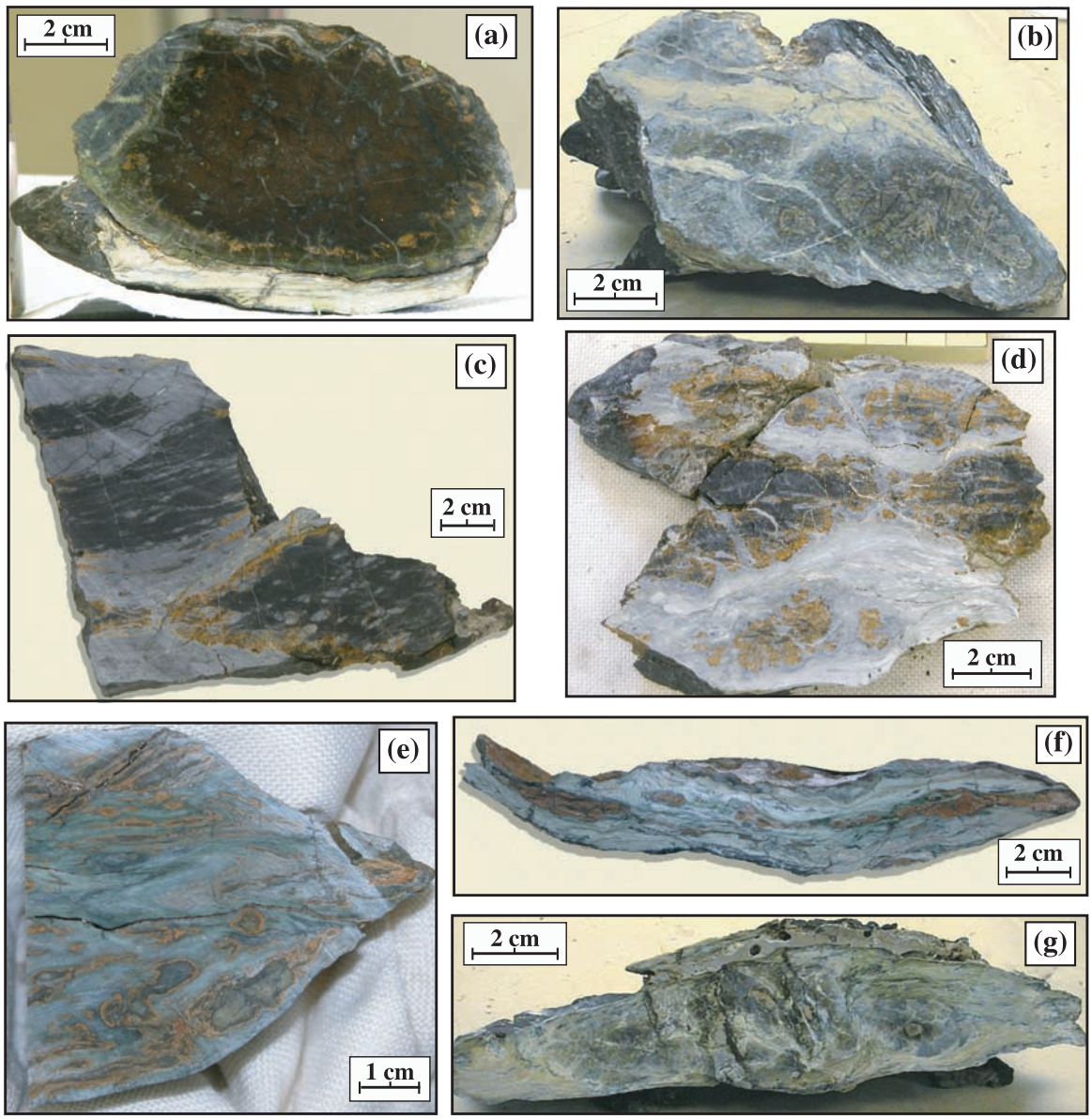

Figure 4. Examples of samples showing progressive deformation and formation of metasomatic talc schists along the detachment fault zone of the south wall of the Atlantis Massif. (a) Sample 3873-1245: less deformed, porphyroclastic serpentinite with thin metasomatic rim of talc-amphibole metasomatism. A thin domain of oxidation separates the metasomatic rim from the serpentinite. A narrow band of highly foliated talc schists (white area) is seen on the bottom of the sample. (b) Sample 3645-1159: serpentinite crosscut by anastomosing vein network filled with talc, amphibole, and chlorite. Relics of mesh-textured serpentinite are pervasively affected by static metasomatism. Samples (c) 3873-1344 and (d) 3873-1124: two examples of metasomatic talc-amphibole-rich bands (light colored domains) enclosing lenses of serpentinite (dark domains). The talc-amphibole assemblages are preferentially oriented parallel to banding in the sample. The serpentinized relicts in sample 3873-1344 (Figure 4c) show crystal-plastic deformation with recrystallized olivine grains and orthopyroxene porphyroclasts (see also Figure 6b). In both samples the rims of the serpentinite domains are partially oxidized. Samples (e) 3863-1425, (f) 3863-1419, and (g) 3645-1225 are examples of typical talc-amphibole schist showing heterogeneous high strain crystal-plastic textures. The synkinematic talc-amphibole assemblages wrap around strongly deformed relicts of serpentinites with oxidized rims (Figures 4e and 4f), locally with rotational-sigmoidal features (Figure 4g), and form sheath-like folds.

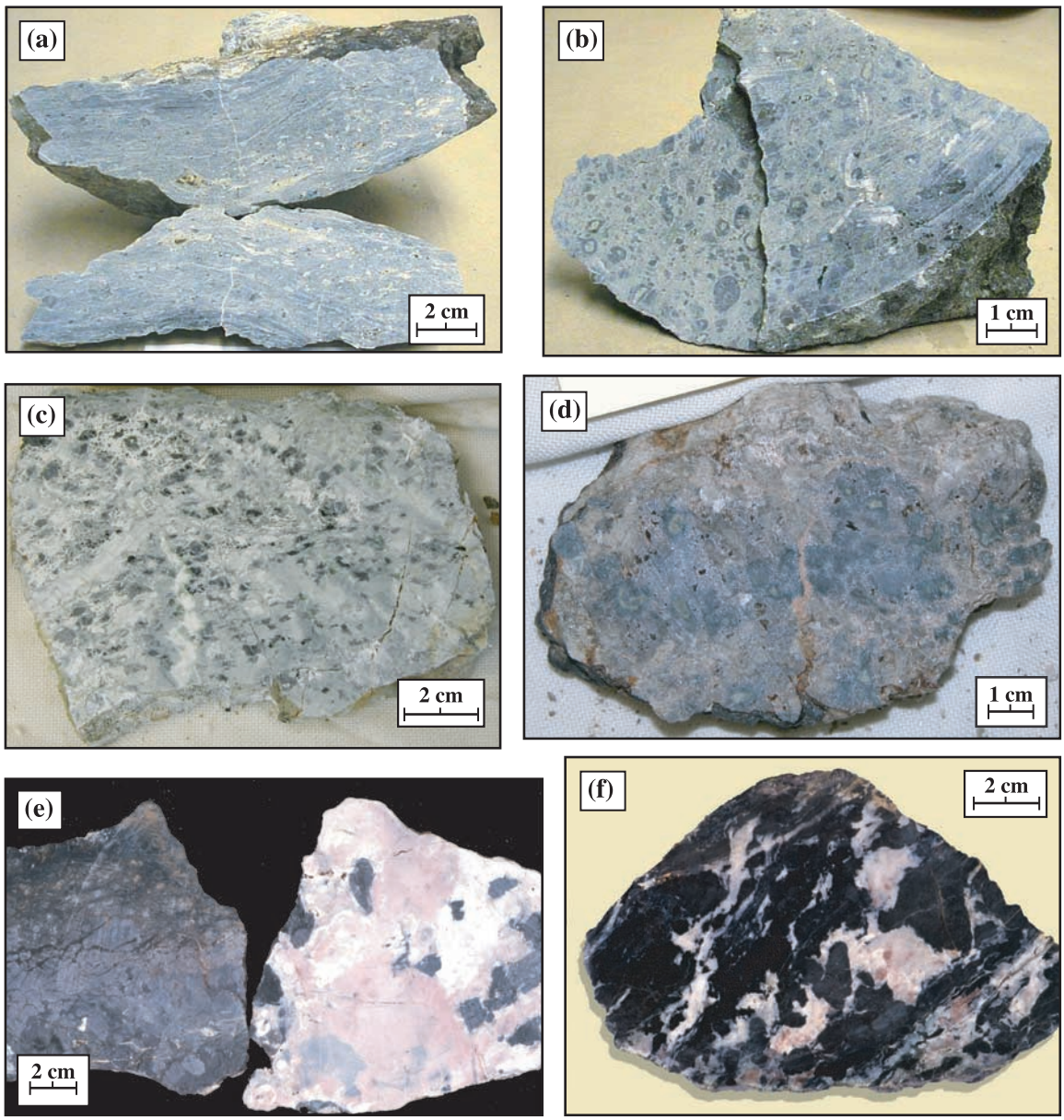

Figure 5. Representative samples of amphibole- and chlorite-rich rocks and rodingites recovered from the south wall of the Atlantis Massif. (a) Sample 3646-1205: typical amphibole-schist showing well-developed mylonitic texture and porphyroclasts. Examples of typical amphibole fels: samples (b) 3647-1359 and (c) 3877-1313. The original protolith is completely transformed to an isotropic network of amphibole crystals. Relics of porphyroclasts remain identifiable and are replaced by (b) fine-grained needles of amphibole, talc and chlorite, or (c) solely by amphibole crystals. (d) Sample 3863-1236: chlorite-rich rock showing an intense static, metasomatic overprinting a brecciated porphyroclastic protolith. (e) Sample 3650-1437: gabbronorite (left) and its rodingite equivalent (right) recovered in the same sample; the whitish-pinkish areas consist of prehenite, clinozoisite, and titanite. (f) 3652-0938 coarse-grained gabbro partially altered to rodingite mineral assemblage (white-pink areas) and showing local shearing.

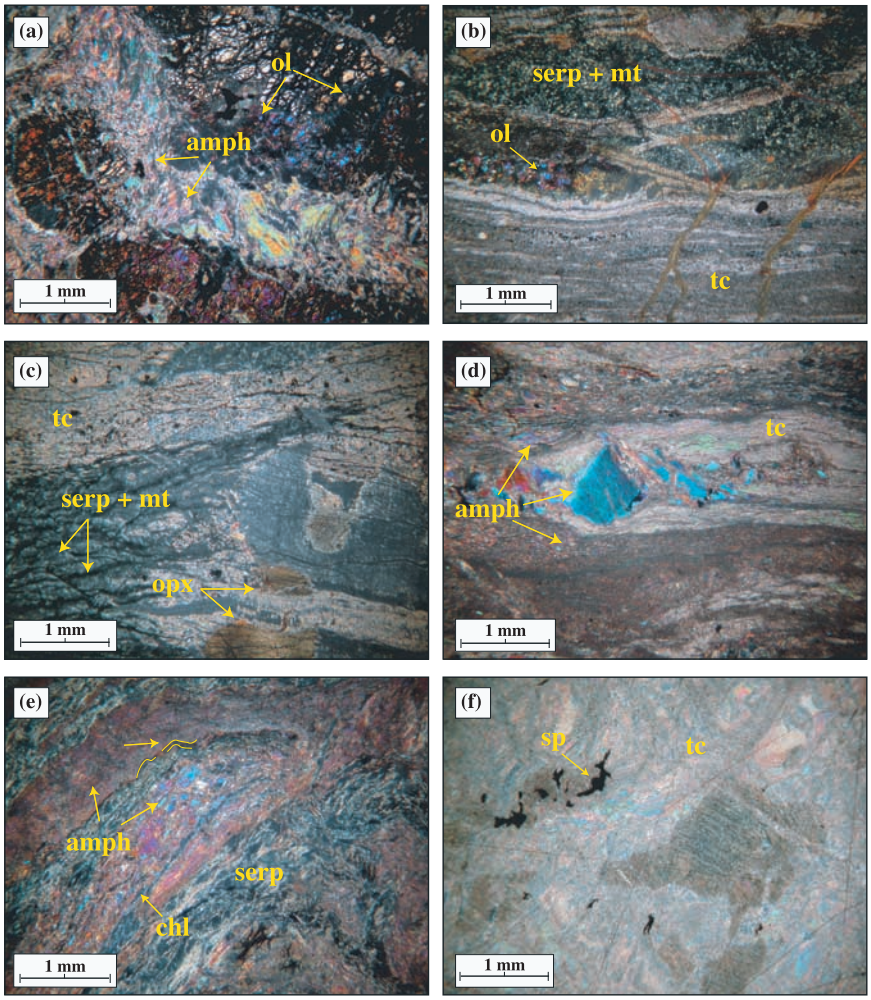

Figure 6. Representative photomicrographs of thin sections of the talc-rich fault rocks, showing characteristic mineral assemblages, fabrics, and microstructures. (a) Sample 3873-1245: incipient talc ± tremolite ± chlorite replacement and vein infill of a partially serpentinized peridotite. (b) Sample 3873-1344: talc-rich layers crosscutting a previously mylonitic serpentinite. (c) Sample 3646-1000: pervasive talc metasomatism associated with talc vein formation; note the orthopyroxene porphyroclast crosscut by the talc vein. Aligned disseminated magnetite grains preserve the original texture of the protolith. (d) Sample 3873-1124: talc schist showing the typical heterogeneous mylonitic texture with alternating bands of fine-grained, dynamically crystallized talc (±amphibole) and ribbons of granular amphibole. (e) Sample 3863-1425: polydeformed talc-amphibole schist showing a crenulated and folded amphibole-rich band. (f) Sample D4-4: Serpentinite statically replaced by talc. Spinel is unaltered, and the orthopyroxene porphyroclast remain recognizable.

overall serpentinization process and metasomatic alteration.

[33] Metasomatic alteration to talc and/or amphibole-rich mineral assemblages is characteristic of the detachment fault zone at the top of the Atlantis Massif and the strongly foliated shear zones at greater depths along the southern wall. Localized heterogeneous deformation and alteration on a micro-scale are observed even in samples that macroscopically show no overprinting and appear to be undeformed (Figures 4 and 6). Local wallrock alteration is associated with hydrothermal veins consisting of varying proportions of Ca-amphibole, chlorite and talc, which in some cases are reactivated and filled with carbonate (e.g., sample 3649-0959). In some samples (e.g., sample 3877-1313), tremolitic amphibole asbestos veins, up to 5–10 cm thick, are observed. Penetrative cataclastic deformation is observed in a few samples recovered during the 2000 cruise close to the top of the massif [*Schroeder and John*, 2004], however our studies of samples collected in 2003 indicate that cataclastic deformation and overprinting to

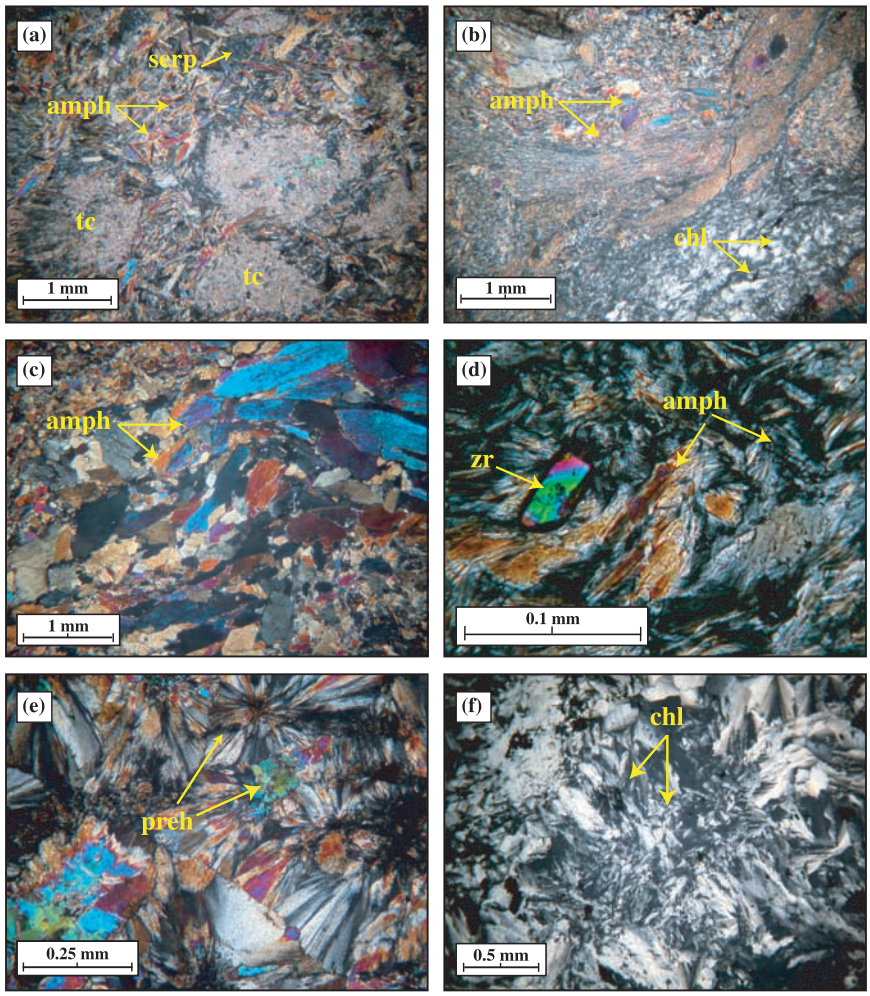

Figure 7. Representative photomicrographs of thin sections of amphibole- and chlorite-rich rocks, showing mineral assemblages, fabrics, and microstructures. (a) Sample 3647-1359: amphibole fels showing amphibole-rich matrix surrounding patches of amphibole ± talc ± chlorite that resemble porphyroclasts. (b) Sample 3865-1245: amphibole schist showing heterogeneously sheared domains wrapping around a deformed porphyroclast (upper left). Fine-grained elongate amphiboles ± fibrous chlorites define a discontinuous foliation; crystals of granular amphiboles are aligned along the irregular foliation and are rotated at a high angle to the overall schistosity. Note the gray, chlorite-rich vein-like zone (lower right). (c) Sample 3863-1355: detail of amphibole fels showing the network of medium- to coarse-grained amphibole. (d) Sample 3646-1205: zircon dispersed in amphibole-rich matrix. (e) Sample 3867-1253: detail of fan-shaped prehnite vein. (f) Sample 3863-1236: fine- to medium-grained gray chlorite forming a monomineralic rock.

greenschist-facies assemblages is minimal in the high strain domains that define most of the detachment shear zone.

[34] Serpentine (lizardite ± chrysotile) occurs as a pre-, syn- and post-metasomatic alteration phase. Late serpentine veins crosscut both the talc-rich shear zones and earlier generations of serpentine, indicating that serpentinization took place in several stages and continued throughout the tectonic evolution of the massif. Recrystallization of lizardite to antigorite locally occurred along millimeter-sized shear zones and produced a fine-grained interlocking texture [*Wick and Whittaker*, 1977] along sub-millimeter-sized planar zones or fan-shaped bundles of bladed serpentine crystals. Moreover serpentine recrystallization and/or new growth of antigorite are observed locally in relatively late slip-fiber veins that post-date the talc schist assemblages.

[35] A late network of aragonite and/or calcite veins and veinlets is widespread. The carbonate veins crosscut all other alteration assemblages and silicate veins, and are most likely related to hydrothermal activity associated with the formation of

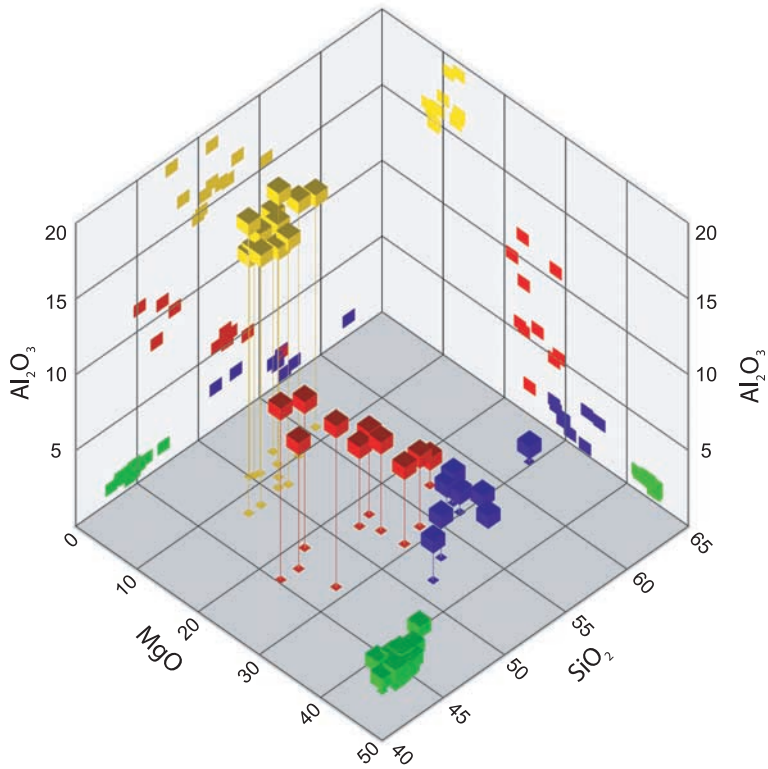

Figure 8. Three-dimensional representation of major element distribution of talc-rich (blue) and amphibole-rich (red) rocks together with AM serpentinites (green) and gabbros (yellow). The talc and amphibole schists show [MgO] and [Al_2O_3] between those of serpentinites and gabbros. In the binary plot MgO versus Al_2O_3 (projection xz), there is a clear inverse correlation between the two elements. Moreover, concentrations of amphibole-rich samples are closer to the AM gabbros and concentrations of talc-rich samples to the AM serpentinites. By contrast, SiO_2 shows no correlation with the other two elements (projections xy and yz), suggesting strong remobilization during the metasomatism. Talc-rich rocks, due to the elevated stoichiometric concentration of Si in the crystal structure, are most enriched in [SiO_2].

the Lost City hydrothermal vent field. Two samples of calcite veins in the basement in the vicinity of the detachment fault near Lost City yielded ^{14}C ages of 32,000 years; samples of the pelagic carbonate cap rocks and carbonate matrix in the sedimentary breccias yielded ages of 25,000 to 34,000 years [*Früh-Green et al.*, 2003]. The radiocarbon ages thus indicate that this latest generation of undeformed carbonate veins probably postdated deformation in the detachment shear zone and thus provides an upper bound on detachment-related slip.

4.1.3. Metasomatic Rocks in the Detachment Shear Zone

[36] The ultramafic and gabbroic rocks recovered along the DSZ and in shear zones on the south wall of the AM show varying degrees of metasomatic alteration to talc-, amphibole-rich, and/or chlorite-rich assemblages. Relict reddish Cr-spinels (associated with ultramafic protoliths), rounded fine-grained oxide ± hydroxide, and opaque minerals are minor components. Plagioclase is distinctly lacking in all of the metasomatic samples investigated in our study, whereas chlorite is widespread. In thin section, chlorite is present as bluish-brown fibrous crystals intergrown with talc and/or amphibole, or as radial aggregates of lamellar crystals (with light gray-white birefringence and colorless in planar light; Figure 7f) that occurs locally in late veins and/or as outer alteration rims on the samples.

[37] The metasomatic rocks have highly variable textures and modal amounts of the characteristic minerals talc, Ca-amphibole and chlorite ± serpentine. This mineral assemblage produces dis-

Table 3. Bulk Rock Major-Element and Trace-Element Compositions of the Gabbroic Rocks From the South Wall of the Atlantis Massif[a]

Sample	3639-1003	3647-1345	3867-1558	3867-1603	3876-1117	3646-1328	3867-1254	3646-1138	D4-6	3873-1544	3649-1257	3876-1215	3867-1607	D4-5	3880-1349	D3-38	3647-1323
Depth, m	1648	1661	748	748	869	2043	843	2393		797	1188	798	751		819		1755
Type	Gabbro	Gabbro	Gabbro	Gabbro	Gabbro	Gabbro	Gabrro	Micro gabbro	Micro gabbro	Gabbro-norite	Gabbro-norite	Pyroxe-nite	Pyroxe-nite	Olivine-gabbronorite	Fe-Ti gabbro	Fe-Ti gabbro	Fe-Ti gabbro
Description	Plagio. neoblasts	Plagio. neoblasts	High-T	High-T	High-T	Plagio. neoblasts	Prehnite, zeolite veins			High-T	Plagio. neoblasts	Low-T (prehnite, zeolite)		High-T and Low-T	High-T amphi		Plagio. neoblasts
Major Elements, weight %																	
SiO_2	51.74	55.19	49.06	49.69	52.36	46.63	47.90	49.76	48.64	44.01	50.32	59.31	42.43	46.88	33.09	32.11	46.63
TiO_2	0.636	0.374	0.612	0.310	0.270	0.309	0.466	1.030	1.296	1.012	1.108	0.437	0.350	1.858	7.910	3.931	3.819
Al_2O_3	15.92	15.35	15.69	18.34	16.65	15.89	15.10	14.83	14.34	17.70	15.83	6.38	14.93	6.95	6.25	13.70	9.43
Fe_2O_3	8.53	6.54	6.40	4.78	4.72	10.02	5.54	10.32	10.68	8.65	8.34	3.65	7.07	9.70	25.04	16.12	17.20
MnO	0.152	0.103	0.065	0.040	0.080	0.523	0.066	0.166	0.142	0.089	0.119	0.077	0.090	0.195	0.330	0.153	0.461
MgO	9.21	7.96	11.97	10.52	9.81	12.08	11.39	8.56	8.16	11.58	8.79	15.29	17.74	21.12	8.95	15.77	9.10
CaO	10.88	9.63	8.60	10.26	11.29	6.96	11.30	12.05	11.81	5.41	11.92	9.33	9.18	8.83	11.54	6.91	8.02
Na_2O	2.69	4.08	2.99	3.00	3.25	3.11	1.88	2.19	2.07	3.35	2.90	1.19	1.14	1.19	1.06	1.10	2.66
K_2O	<d.l.	0.08	0.60	0.22	<d.l.	0.04	1.13	0.06	0.06	0.10	0.07	0.09	0.18	0.04	<d.l.	0.08	0.08
P_2O_5	0.03	0.02	<d.l.	<d.l.	<d.l.	0.01	0.04	0.07	0.12	0.13	0.04	0.01	<d.l.	0.02	1.73	2.50	1.07
LOI*	0.19	0.66	3.40	2.63	1.42	4.53	4.38	0.76	1.69	6.91	0.45	2.95	6.71	3.46	2.57	6.30	1.42
Total	99.95	99.98	99.39	99.79	99.85	100.09	99.18	99.80	99.00	98.94	99.88	98.71	99.82	100.26	98.47	98.67	99.87
CO_2, wt%	0.004	0.008	0.010	0.004	0.003	0.539	0.006	0.004	0.579	0.329	0.017	0.04	0.002	0.074		0.02	0.018
Density, g/cm^3												2.79	2.88				
Trace Elements, ppm																	
V	157	143	273	151	172	124	222	243	268	200	189	134	221	161	452	116	264
Cr	137	83	74	57	210	197	113	249	162	89	506	1810	83	1050	40	27	202
Co	36	31	47	35	33	44	38	51	47	31	41	28	47	41	73	74	59
Ni	186	134	310	274	277	274	209	135	110	220	207	445	601	501	309	891	255
Cu	28	<d.l.	<d.l.	<d.l.	<d.l.	<d.l.	<d.l.	76	<d.l.	25	35	<d.l.	<d.l.	<d.l.	56	<d.l.	106
Zn	59	39	<d.l.	<d.l.	<d.l.	141	<d.l.	89	66	61	44	<d.l.	<d.l.	<d.l.	126	<d.l.	68
Ga	14	17	13	14	14	14	12	15	15	18	15	8	15	9	27	20	18
Rb	3	<d.l.	3	1	<d.l.	<d.l.	6	<d.l.	<d.l.	<d.l.	<d.l.	<d.l.	1.80	<d.l.	1	<d.l.	<d.l.
Sr	97	115	120	139	119	80	137	66	143	124	112	10	13	17	50	49	77
Y	15.5	85.6	14.3	8.3	14.3	8.6	14.8	25.3	31.2	13.6	17.5	35	13	47	192	121	73
Zr	19	45	10	12	11	11	15	47	79	15	16	130	8	78	132	77	57
Nb	10.0	6.9	<d.l.	<d.l.	0.3	5.2	0.9	7.4	4.7	0.4	4.0	1.09	<d.l.	2.18	13.5	5.0	6.24
Cs	<d.l.	<d.l.	<d.l.			<d.l.	<d.l.	<d.l.	<d.l.	<d.l.	<d.l.	<d.l.	<d.l.	<d.l.	<d.l.	<d.l.	<d.l.
Ba	10	18	219	112	5	4	164	4	6	14	7	5.1	3.6	<d.l.	5	<d.l.	13.1
La	0.71	6.60	0.67	0.82	0.92	0.42	1.00	1.42	2.58	0.84	1.01	1.13	1.08	3.70	11.00	33.17	8.16
Ce	2.28	22.55	2.07	2.23	3.19	1.55	2.97	4.82	8.04	2.19	3.30	4.70	3.48	15.69	42.20	93.05	26.12

Table 3. (continued)

Sample	3639-1003	3647-1345	3867-1558	3867-1603	3876-1117	3646-1328	3867-1254	3646-1138	D4-6	3873-1544	3649-1257	3876-1215	3867-1607	D4-5	3880-1349	D3-38	3647-1323
Depth, m	1648	1661	748	748	869	2043	843	2393		797	1188	798	751		819		1755
Type	Gabbro	Gabbro	Gabbro	Gabbro	Gabbro	Gabbro	Gabrro	Micro gabbro	Micro gabbro	Gabbro-norite	Gabbro-norite	Pyroxe-nite	Pyroxe-nite	Olivine-gabbronorite	Fe-Ti gabbro	Fe-Ti gabbro	Fe-Ti gabbro
Description	Plagio. neoblasts	Plagio. neoblasts	High-T	High-T	High-T	Plagio. neoblasts	Prehnite, zeolite veins			High-T	Plagio. neoblasts	Low-T (prehnite, zeolite)		High-T and Low-T	High-T amphi		Plagio. neoblasts
Pr	0.43	4.04	0.34	0.35	0.58	0.29	0.51	0.88	1.27	0.37	0.58	0.92	0.59	2.83	8.70	13.42	4.26
Nd	2.80	23.66	2.20	1.84	3.08	1.64	3.08	5.56	8.01	2.36	3.71	5.85	3.11	16.51	54.40	70.24	24.00
Sm	1.34	9.03	1.14	0.69	1.18	0.68	1.30	2.41	3.17	1.15	1.63	2.59	1.16	6.13	21.80	20.63	8.94
Eu	0.903	1.000	0.657	0.492	0.460	0.389	0.655	0.940	1.135	1.261	0.925	0.61	0.607	2.617	4.990	4.502	2.709
Gd	2.11	11.95	1.95	1.01	1.64	0.99	1.92	3.57	4.27	1.80	2.45	4.15	1.61	8.34	29.00	26.62	12.84
Tb	0.43	2.36	0.42	0.20	0.32	0.22	0.42	0.71	0.86	0.39	0.49	0.89	0.31	1.52	5.05	4.12	2.22
Dy	2.87	14.97	2.88	1.37	2.23	1.50	2.69	4.67	5.66	2.69	3.28	6.03	2.15	9.69	32.20	24.33	14.66
Ho	0.64	3.26	0.60	0.29	0.48	0.34	0.55	1.00	1.19	0.58	0.73	1.28	0.46	2.04	6.54	4.86	2.85
Er	1.88	9.45	1.90	0.88	1.48	1.04	1.80	2.96	3.80	1.75	2.09	4.06	1.38	6.11	17.60	13.66	8.65
Tm	0.283	1.352	0.279	0.131	0.228	0.165	0.281	0.445	0.556	0.258	0.315	0.59	0.206	0.857	2.420	1.714	1.223
Yb	1.81	8.45	1.72	0.91	1.55	1.07	1.64	2.76	3.33	1.66	2.00	3.45	1.38	5.15	15.30	9.09	7.35
Lu	0.290	1.230	0.259	0.144	0.240	0.172	0.237	0.434	0.469	0.250	0.312	0.49	0.22	0.77	2.230	1.27	1.07
Hf	0.70	2.10	0.55	0.34	0.42	0.51	0.80	1.49	2.31	0.63	0.80	3.65	0.32	3.10	4.4	2.8	2.31
Ta	0.21	0.14	<d.l.	0.01	0.03	0.05	<d.l.	0.13	0.13	<d.l.	0.09	0.06	<d.l.	0.15	0.92	0.15	0.40
Pb	<d.l.	<d.l.	<d.l.			<d.l.	<d.l.	<d.l.	<d.l.	<d.l.	<d.l.	<d.l.	<d.l.	<d.l.	<d.l.	<d.l.	<d.l.
Th	0.11	0.33	<d.l.	0.01	0.04	<d.l.	<d.l.	0.08	0.23	<d.l.	<d.l.	<d.l.	0.01	0.13	0.07	0.34	0.28
U	0.02	0.11	0.01	<d.l.	0.02	0.03	0.01	0.14	0.10	0.05	0.03	0.02	0.02	0.03	0.37	0.10	0.16
$[La/Yb]_N$	0.27	0.53	0.26	0.61	0.40	0.27	0.41	0.35	0.53	0.34	0.34	0.22	0.53	0.49	0.49	2.48	0.75
Eu/Eu*	1.63	0.29	1.33	1.80	1.01	1.44	1.26	0.97	0.94	2.67	1.41	0.56	1.35	1.12	0.60	0.59	0.77
$[La/Sm]_N$	0.33	0.46	0.36	0.74	0.49	0.38	0.48	0.37	0.51	0.46	0.39	0.27	0.58	0.38	0.32	1.00	0.57
$[Gd/Yb]_N$	0.94	1.14	0.91	0.90	0.86	0.75	0.95	1.05	1.04	0.88	0.99	0.98	0.94	1.31	1.53	2.37	1.41
$[Dy/Er]_N$	0.99	1.03	0.99	1.01	0.98	0.94	0.97	1.03	0.97	1.00	1.02	0.97	1.01	1.03	1.19	1.16	1.10

[a] Notes: <d.l., below detection limit; LOI, loss on ignition; Eu/Eu*, $Eu_N/(Sm_N*Gd_N)^{1/2}$; Eu_N, Sm_N, and Gd_N are the chondrite-normalized concentrations of Eu, Sm, and Gd, respectively. Plagio., plagioclase.

tinctly light- to white-colored rocks with a soapy feel that are similar to "steatites" or "soapstones" common in Alpine peridotite terrains (Figure 4). No distinction in mineralogy or deformation behavior could be found between samples collected from the detachment shear zone and those from discrete, anastomosing shear zones that cut both the DSZ as well as the deeper basement rocks. Talc and amphibole are the most abundant mineral phases and are present in varying inverse proportions in rocks showing a large variation in the degree of deformation. Depending on the degree of deformation, the talc- or amphibole-rich metasomatic rocks fall between two end-members that can be defined as schist or fels. Although crosscutting relationships point to temporal variations in deformation, the similarities in mineralogies, textures and metasomatic overprinting suggest that deformation and alteration occurred under similar greenschist-facies metamorphic conditions.

4.1.3.1. Talc-Rich Fault Rocks

[38] The talc-rich rocks commonly preserve precursor ribbon or mesh serpentine textures and contain less amphibole. The metasomatic mineral assemblages in some cases preserve the original porphyroclastic texture of the serpentinite protolith, in which case, these are referred to as talc-amphibole serpentinites (Figures 4 and 6; Table 4). Serpentine is present in relict domains (Figures 6a, 6b, and 6c), but it is also observed as newly formed crystals intergrown with talc or as localized pockets of recrystallized antigorite with non-pseudomorphic interlocking texture (Figure 6e). Talc occurs as a replacement product of groundmass serpentine and may occur together with tremolite ± chlorite as alteration products of bastite pseudomorphs after orthopyroxene. Incipient replacement of serpentine by talc is initiated along serpentine bands defining ribbon textures and mesh rims, along microfractures in the serpentinite, or as alteration rims and halos that are related to a series of talc-amphibole-chlorite-rich veins that reach a few centimeters in thickness (Figures 6a, 6b, and 6c).

[39] Strongly foliated talc-amphibole schists (e.g., samples 3645-1225, 3863-1419, and 3863-1425; Figures 4e, 4f, 4g, 6d, and 6e) are the most distinctive fault rocks at the Atlantis Massif. They typically show a heterogeneous mylonitic texture (following *Passchier and Trouw* [1998]) characterized by a strong foliation defined by shape preferred orientations parallel to the orientation of the DSZ, which locally is overprinted by a crenulation lineation (e.g., Figure 6e). The mylonitic planar foliation is composed of alternating layers of variably sized, synkinematic talc, Ca-amphibole and chlorite and lenses, defined as ribbons (following *Passchier and Trouw* [1998]), in which strongly deformed mantled orthopyroxene porphyroclasts are embedded. The pyroxene ribbons are commonly altered to patches of talc + amphibole ± chlorite and show strong undulose extinction, subgrain structures and dynamic recrystallization, mainly along the rim of the ribbons. Kinematic indicators in the talc-amphibole schists include asymmetrical foliation patterns, pressure shadows around pyroxene porphyroclasts, and local folds and indicate normal slip, that is, top-to-east (toward the spreading axis) or southeast (toward the transform). Crenulation lineation is defined by amphibole neoblasts that form at a high angle to foliation, suggesting that amphibole continued to grow after the formation of the mylonitic foliation.

[40] Progressive deformation and formation of talc schist is particularly evident in samples, in which lenses of serpentinite are enclosed by mm-sized, variably oxidized rims, and in turn, are surrounded by white, sheared domains that consist of metasomatic mineral assemblages (Figure 4). The lens-shaped central domains characteristically have a lower degree of serpentinization and may contain enclaves of relatively fresh olivine relicts (Figures 6a and 6b). In contrast, the sheared domains occur as localized sigmoidal zones that define a variable and irregular foliation. With progressive deformation, the lens-shaped domains become increasingly elongate and talc-rich rims form a well-developed schistosity. Small-scale folds, as observed in sample 3863-1425 (Figures 4e and 6e), preserve this progressive alteration history and reflect high-strain deformation during metasomatism and detachment faulting.

[41] A small number of the samples can be classified as talc-rich fels. These samples lack a penetrative high-strain deformation fabric but may show brittle deformation features, commonly in the form of fractures and veins. They are dominated by static crystallization of fine-grained talc, Ca-amphibole ± chlorite, which variably replace the precursor mineral phases. Sample D4-4 is an example of solely static replacement by talc, characterized by coarse-grained pseudomorphic talc domains, in which the ribbon texture of serpentine,

Table 4. Bulk Rock Major-Element (wt.%) and Trace-Element (ppm) Compositions of Talc-Rich Metasomatic Rocks, and Average Serpentinite Compositions of 24 Samples From the South Wall of the Atlantis Massif[a]

Sample	3645-1225	D3-46	3863-1419	3863-1425	3863-1526	3873-1124	D4-4	3642-1309	Average	StDev
Depth, m	955		794	794	778	959		1751		
Type	Talc schist	Talc schist	Talc-amph schist	Talc-amph schist	Talc-amph schist	Talc-amph schist	Talc fels	Talc-amph fels	Serp.	Serp.
					Major Elements, weight %					
SiO_2	53.84	49.69	53.96	46.63	51.54	52.95	58.87	53.11	38.73	0.82
TiO_2	0.024	0.100	0.071	0.058	0.021	0.009	0.007	0.061	0.023	0.02
Al_2O_3	0.66	2.65	1.91	2.46	0.45	1.33	1.05	1.63	0.95	0.15
Fe_2O_3	3.42	8.65	3.73	5.32	4.97	4.09	6.27	10.00	8.38	0.71
MnO	0.106	0.055	0.054	0.055	0.036	0.051	0.069	0.110	0.087	0.02
MgO	28.57	31.34	26.70	32.17	29.95	27.85	27.90	26.81	38.02	0.63
CaO	6.09	0.92	8.06	3.55	3.05	7.15	0.12	2.60	0.19	0.28
Na_2O	0.29	0.13	0.50	0.32	0.22	0.26	0.16	0.24	0.09	0.02
K_2O	0.06	0.04	0.02	0.05	0.02	0.01	0.04	0.05	0.02	0.01
P_2O_5	0.02	0.04	0.01	0.04	0.05	0.01	0.01	0.02	0.04	0.02
LOI*	6.92	6.17	4.94	9.24	9.95	6.13	5.26	5.51	13.19	0.62
Total	99.99	99.77	99.96	99.89	100.24	99.85	99.77	100.14	99.91	0.33
CO_2, wt%	0.19	0.03	0.01	0.01	1.84	0.14	0.01	0.02	0.11	0.19
Density, g/cm^3			2.62	2.65	2.76				2.57	0.10
					Trace Elements, ppm					
V	30	28	40	45	51	38	19	55	45	7
Cr	1070	1660	1420	1450	1570	1890	2000	2440	2467	396
Co	40	61	36	66	67	50	44	56	92	9
Ni	1000	1320	858	1300	1080	898	1170	1420	1852	241
Cu	<d.l.	<d.l.	28	<d.l.	11	<d.l.	<d.l.	23	13	14
Zn	50	<d.l.	<d.l.	<d.l.	<d.l.	32	52	147	36	11
Ga	2	4	3	3	1	3	2	5	2	1
Rb	<d.l.	<d.l.	<d.l.	<d.l.	2	<d.l.	<d.l.	<d.l.	<d.l.	
Sr	7	<d.l.	6	5	29	7	<d.l.	5	11	19
Y	2.6	17.1	2.8	2.0	1.3	1.2	<d.l.	3.5	1.2	1.1
Zr	<d.l.	92	6	<d.l.	<d.l.	<d.l.	<d.l.	<d.l.	4	5
Nb	1.0	1.0	1.0	0.9	<d.l.	0.6	<d.l.	1.2	0.1	0.05
Cs	<d.l.	<d.l.	<d.l.	<d.l.	0.2	<d.l.	<d.l.	<d.l.	<d.l.	
Ba	<d.l.	<d.l.	<d.l.	<d.l.	<d.l.	<d.l.	<d.l.	<d.l.	8	4
La	0.09	1.41	0.47	0.45	0.20	0.24	<d.l.	0.66	0.17	0.12
Ce	0.28	4.91	1.51	1.14	0.33	0.62	0.08	1.55	0.47	0.37
Pr	0.05	0.82	0.26	0.15	0.05	0.09	<d.l.	0.23	0.08	0.06
Nd	0.41	4.80	1.43	0.79	0.33	0.46	0.06	1.18	0.37	0.28
Sm	0.20	1.76	0.46	0.26	0.12	0.16	0.04	0.37	0.13	0.08
Eu	0.077	0.336	0.249	0.119	0.073	0.093	<d.l.	0.128	0.046	0.022
Gd	0.34	2.43	0.50	0.30	0.14	0.16	0.03	0.46	0.14	0.08

Table 4. (continued)

Sample	3645-1225	D3-46	3863-1419	3863-1425	3863-1526	3873-1124	D4-4	3642-1309	Average	StDev
Depth, m	955		794	794	778	959		1751		
Type	Talc schist	Talc schist	Talc-amph schist	Talc-amph schist	Talc-amph schist	Talc-amph schist	Talc fels	Talc-amph fels	Serp.	Serp.
Tb	0.08	0.48	0.09	0.06	0.03	0.03	<d.l.	0.09	0.03	0.02
Dy	0.50	3.16	0.54	0.37	0.20	0.23	0.03	0.53	0.18	0.12
Ho	0.10	0.71	0.11	0.08	0.04	0.05	<d.l.	0.11	0.04	0.02
Er	0.33	2.25	0.34	0.25	0.13	0.17	0.03	0.35	0.13	0.08
Tm	0.052	0.345	0.049	0.035	0.023	0.026	<d.l.	0.055	0.027	0.012
Yb	0.30	2.08	0.32	0.24	0.15	0.17	0.02	0.31	0.16	0.07
Lu	0.043	0.322	0.046	0.036	0.020	0.023	0.004	0.046	0.026	0.01
Hf	<d.l.	2.6	0.3	0.2	0.1	0.1	0.1	<d.l.	0.1	0.1
Ta	<d.l.	0.01	<d.l.	<d.l.	<d.l.	<d.l.	<d.l.	<d.l.	0.03	0.02
Pb	<d.l.	<d.l.	<d.l.	<d.l.	<d.l.	<d.l.	<d.l.	13	<d.l.	
Th	<d.l.	0.10	<d.l.	<d.l.	<d.l.	<d.l.	<d.l.	<d.l.	0.16	0.49
U	0.73	0.03	0.09	0.41	0.32	0.22	0.02	0.09	0.66	0.25
$[La/Yb]_N$	0.21	0.46	0.98	1.30	0.88	0.96		1.44	0.72	
Eu/Eu*	0.90	0.50	1.57	1.29	1.74	1.74		0.94	1.00	
$[La/Sm]_N$	0.29	0.50	0.63	1.09	1.05	0.92		1.13	0.78	
$[Gd/Yb]_N$	0.91	0.94	1.25	1.04	0.72	0.80	0.99	1.19	0.74	
$[Dy/Er]_N$	0.98	0.91	1.04	0.99	0.98	0.89	0.78	0.99	0.87	

[a] Notes: <d.l., below detection limit; LOI, loss on ignition; Eu/Eu*, $Eu_N/(SmN*GdN)^{1/2}$; Eu_N, Sm_N, and Gd_N are the chondrite-normalized concentrations of Eu, Sm, and Gd, respectively. Serp., serpentinite.

the pyroxene porphyroclasts, and relicts of Mg-Cr spinel are preserved (Figure 6f).

4.1.3.2. Amphibole-Rich Fault Rocks

[42] In contrast to the talc-rich rocks, alteration to amphibole-rich assemblages has commonly obliterated the primary textures and precursor mineral parageneses, preventing an unequivocal petrographic determination of the protoliths. Moreover the amphibole-rich rocks show alteration textures that are distinct from the talc-rich rocks. They consist of well-crystallized, elongate and often aligned amphibole that wraps around lenses and patches of amphibole ± chlorite that resemble porphyroclasts (Figures 7b and 7c). Some of these lenses are conceivably pseudomorphs after pyroxene porphyroclasts. The porphyroclasts are generally deformed and elongate, commonly bent, and display a patchy, undulose extinction (Figure 7b). Acicular grains of amphibole locally define pressure shadows around the crystals and define the foliation. Talc is typically absent in these rocks or occurs only locally together with fine-grained needles of amphibole and chlorite as pseudomorphs of orthopyroxene porphyroclasts (e.g., in samples 3647-1359 or 3873-1250, Figures 5b and 7a).

[43] Sample 3865-1245 (Figure 7b) is a representative example of amphibole schist and consists of heterogeneous, sheared domains that wrap around rare altered and kinked porphyroclasts. Fine-grained elongate amphiboles ± fibrous bluish chlorites define a discontinuous foliation and locally form microfolds. Crystals of granular fine- to medium-grained, partially kinked amphiboles are aligned along the irregular foliation and are rotated at a high angle to the overall schistosity. A late, up to 2 mm thick, gray chlorite-rich (±serpentine and magnetite) vein-like zone, with well-developed foliation (concordant with the amphibole foliation) crosscuts the central part of the sample.

[44] A number of samples (3863-1157, 3865-1355, 3877-1313, 3647-1359; Figures 5b, 5c, 7a, and 7c), defined here as amphibole fels, are dominated by static isotropic growth of medium to coarse-grain amphibole. In these samples, the original protolith is particularly difficult to determine. For example, sample 3865-1355 (Figure 7c) has a primary porphyroclastic texture, in which the primary minerals as well as the matrix are completely replaced by tremolitic amphibole. This could have been a pyroxenite or a pyroxene-rich layer in a coarse-grained gabbroic rock. Sample 3877-1313 contains chromium spinel, which points to a peridotite protolith, however, the chemistry of the sample shows major deviations from the serpentinite chemistries and thus suggests either extensive mass transfer or a ''mixed'' protolith of gabbro and peridotite (possibly troctolitic in composition). The association of the amphibole-rich rocks with chlorite-rich samples (Figures 5d and 7f) suggests that they may be the product of ''blackwall'' alteration that typically form at the contacts between serpentinized peridotite and silica-rich mafic rocks in ophiolites (see below) [e.g., *Frost*, 1975; *Evans*, 1977].

[45] Many of the amphibole-rich samples have zircon crystals ± prismatic apatite as accessories minerals (Figure 7d). Apatite and zircon are common in veins and local domains in serpentinized peridotites and lower crustal gabbros in other oceanic core complexes and in exposed ultramafic rocks at slow- and ultra-slow spreading ridges. For example, they have been identified in hydrothermal veins in serpentinized peridotites from ODP Hole 920 [*Karson and Lawrence*, 1997], in gabbroic veins in serpentinized peridotite from ODP Holes 1270A, 1270C, and 1270D [*Kelemen et al.*, 2004], in gabbroic veins and dikelets in serpentinized peridotite dredged in the Mid-Atlantic Ridge axial valley at 15°37′N and 16°52′N [*Cannat et al.*, 1992], and in gabbros from ODP Hole753B [*Stakes et al.*, 1991; *Vanko and Stakes*, 1991]. Zircons occur in close association with amphibole even if clear textural relationships between the two are lacking. In the AM samples, the largest and most abundant zircons are found in sample 3646-1205 (Figure 7d) [*Schroeder and John*, 2004]; smaller grains and less abundant occurrences are observed in many of the other amphibole-rich samples.

[46] Electron microprobe analyses indicate that the chlorites in the talc- and amphibole-rich fault rocks have compositions that lie in the chamoisite-clinochlore series (according to AIPEA nomenclature [*Bailey*, 1980]; Table 2). The secondary amphiboles in these rocks are typically actinolitic to tremolitic in composition, according to the classification of *Leake* [1978], but show a greater variability in composition in the amphibole-rich fault rocks (Table 1). As discussed by *Schroeder and John* [2004], amphiboles that pseudomorph pyroxenes contain higher Al^{IV} and (Na + K) contents compared to blades of amphiboles that are commonly found in association with chlorite. In the amphibole-rich fault rocks, actinolite is

most common but also occurs together with edenitic and Mg-hornblenditic amphiboles as well as Fe-Mg amphiboles (anthophyllite or cummingtonite; Table 1). For example, sample 3647-1359 (Figure 7a) consists of a network of prismatic amphibole that microscopically appears to be Fe-poor actinolite with a rim of greenish Fe-rich actinolite. Microprobe analyses of this sample identified submillimeter-sized domains of Fe-Mg amphiboles, with compositions similar to anthophyllite or cummingtonite, alternating with actinolitic domains (Table 1). The coexistence of Ca-amphiboles with monoclinic and/or orthorhombic Fe-Mg amphiboles correspond to miscibility gaps in amphibole composition space, and has been described repeatedly [e.g., *Deer et al.*, 1997; *Müller et al.*, 2003]. Although anthophyllite and cummingtonite are commonly considered evidence for temperatures >600°C, little is known of their stability in microdomains with Ca-amphiboles. However, one sample (3646-1205) contains minor amounts of Ti-rich edenite that could be related to high-temperature metamorphism or early melt impregnation.

4.1.3.3. Chlorite-Rich, "Blackwall" Alteration Zones

[47] Samples 3863-1236 and 3639-1415 are characterized by monomineral static alteration to isotropic chlorite. Sample 3863-1236 (Figures 5d and 7f) is composed entirely of gray Fe-rich clinochlore (Table 2) that occurs as fine- to medium-grained, fan-shaped aggregates or as fine-grained fibrous crystals. In sample 3839-1415, amphibole is present in small amounts. *Miyashiro et al.* [1979] dredged similar metasomatic rocks along the Atlantis Fracture Zone at 30°04′N at a depth of 4140 m and attributed the chlorite-rich monomineralic rocks to intense metasomatism of (cumulate) metagabbros characteristic of deformation and metamorphism in a transform fault setting. Recovery of the AM metasomatic sequences within a geologically well-defined context of a detachment shear zone now allows us to re-evaluate these original interpretations.

[48] At the Atlantis Massif, the chlorite-rich rocks most likely represent reaction zones between mafic and ultramafic rocks during the tectonic and metamorphic evolution of the detachment shear zone. Conversion of a multicomponent polymineralic rock to a monomineralic rock during metasomatism is typical of "blackwall" reaction zones, composed of pure chlorite and/or pure talc domains, that form between peridotite and relatively silica-rich wall rocks in ophiolite terrains and in metamorphic belts [e.g., *Chidester*, 1962; *Frost*, 1975; *Bach et al.*, 2004]. In some terrains, blackwalls consist primarily of monomineralic chlorite as the "inner" alteration zones close to the contact with ultramafic rocks and is associated with rodingite in the "outer" alteration zones. These metasomatic sequences are commonly interpreted as evidence for mass transfer under low-grade metamorphic conditions [*Frost*, 1975; *Evans*, 1977]. The presence of distinct samples dominated by talc, amphibole, or chlorite and their association with rodingites at the Atlantis Massif strongly suggests that similar metasomatic processes were active over a range of conditions that developed during the evolution of the DSZ.

4.2. Geochemistry

[49] Major- and trace element data of the metasomatic rocks are reported in Tables 4 and 5 and are compared with the compositional field for AM serpentinites and gabbros in Figures 8 through 11. The bulk rock geochemistries of the basement rocks reflect the differences in mineralogies discussed above and allow the two groups of metasomatic rocks in the fault zones to be distinguished: a group rich in talc and a group dominated by amphibole. The geochemistries of the two groups show no significant correlation with the degree of deformation, but rather reflect variations in modal abundances of the main minerals talc, amphibole and chlorite. This suggests that the mineralogies, and thus the bulk rock compositions, were controlled by the chemical composition of the protolith and/or hydrothermal fluid and are independent of degree of deformation.

[50] Compared to the serpentinized ultramafic protoliths, both groups of metasomatic rocks have higher densities, consistently higher values of SiO_2, Al_2O_3, CaO, TiO_2, and Na_2O, and lower MgO, total Fe (as Fe_2O_3) and water contents, based on loss-on-ignition (LOI). On the other hand, compared to the gabbroic rocks, they are depleted in Al_2O_3, CaO, total Fe and Na_2O, are enriched in MgO, and are slightly enriched in SiO_2 (especially the talc-rich samples; Figures 8 and 9).

[51] The two groups of metasomatic rocks differ substantially in their trace element and Rare Earth Element (REE) distribution (Figures 10 and 11). Both groups have characteristically high absolute concentrations of Cr, Ni, V, and Co; whereby the amphibole-rich samples have lower Cr and Ni contents and higher V contents than the talc-rich samples (Tables 4 and 5). However, compared to

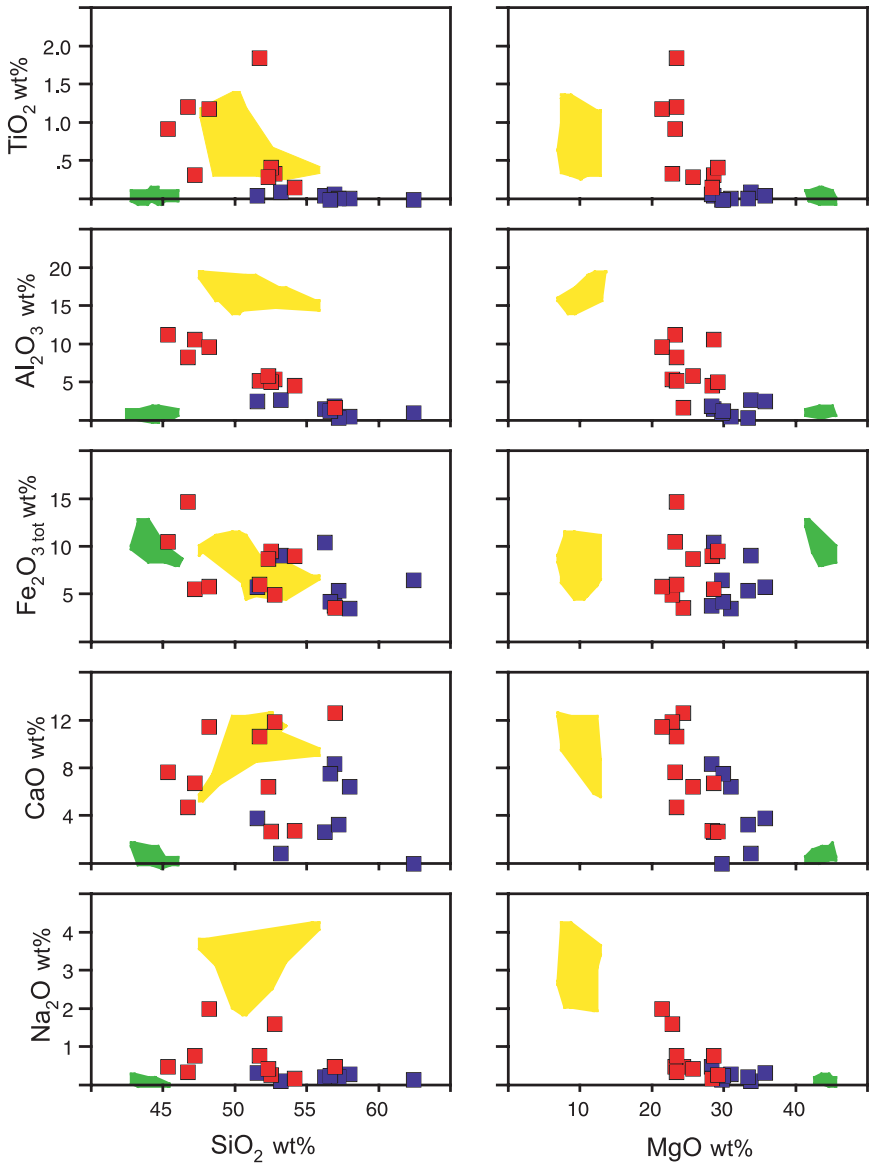

Figure 9. Harker-type diagrams showing chemical variations in major elements of the talc-rich (blue symbols) and amphibole-rich (red symbols) AM rocks. Green and yellow shaded areas show the range of compositions of the non-metasomatic serpentinites and gabbros, respectively. MgO shows an inverse correlation with CaO, Al_2O_3, and Na_2O; SiO_2 shows no correlation with the other major elements, suggesting a strong remobilization of silica during metasomatism. With the exception of MgO and $Fe_2O_{3\ tot}$, the talc-rich rocks are enriched in major elements compared to the AM serpentinites. The amphibole-rich rocks have higher MgO contents but have lower or similar concentrations of the other major elements compared with the AM gabbros.

the serpentinite protoliths, both groups have lower Cr, Ni, and Co concentrations; V contents are similar in the talc-rich samples but higher in the amphibole-rich samples. An opposite relationship is observed relative to the gabbroic rocks: the metasomatic rocks are enriched in Cr, Ni, and Co, and are depleted in V compared to the gabbros. Furthermore, both groups are distinctly enriched in almost all trace and REEs relative to the serpentinite protoliths (Figure 11a), with the exception of U and Pb contents (Tables 4 and 5), which are lower (or the same) in the metasomatic rocks compared to the serpentinite and are comparable or higher than in the gabbros.

[52] Many of the amphibole-rich samples show anomalous enrichments in Zr, Y and Hf (e.g., up to 326 ppm Zr, 153 ppm Y, and 10 ppm Hf in sample 3846-1205; Table 5). Only one sample (D3-46) of the talc-rich group shows comparable

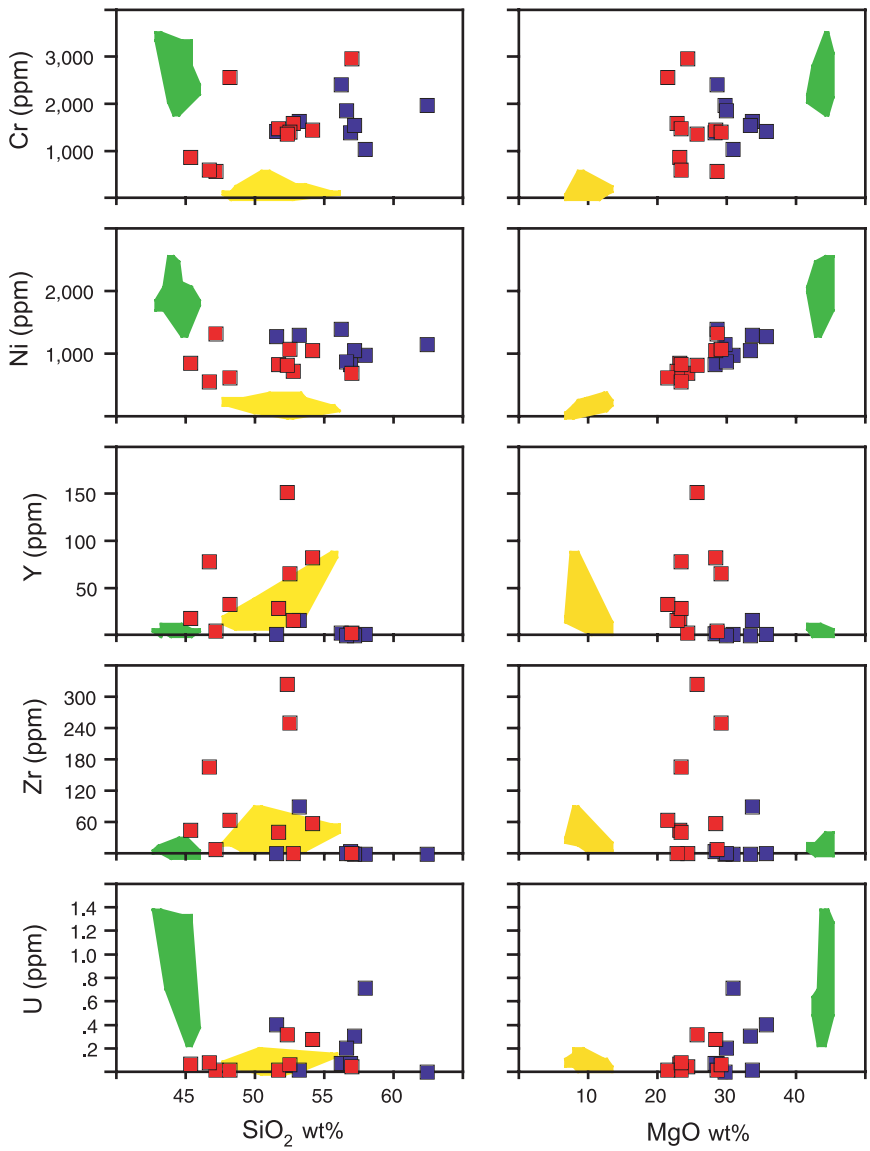

Figure 10. Harker-type diagrams showing chemical variations in trace elements of the talc-rich (blue symbols) and amphibole-rich (red symbols) rocks from the Atlantis Massif. Green and yellow shaded areas show range of compositions of the AM serpentinites and gabbros, respectively. MgO contents correlate with Cr_2O_3, NiO, and U. As with variations in major element compositions, SiO_2 shows no correlation with other trace elements. The amphibole-rich rocks show the highest concentrations of Zr and Y.

values (92 ppm Zr, 17 ppm Y, and 3 ppm Hf; Table 4). Such high values of Zr, Y and Hf are not found in any of the serpentinite protoliths and are rarely observed in the gabbros (e.g., samples 3647-1345 and D4-6; Table 3). The Fe-Ti gabbros are derived from the most evolved melts at the Atlantis Massif and are the only samples that consistently have high values of Zr and Y (e.g., 132 ppm Zr, 192 ppm Y and 4 ppm Hf in sample 3880-1349; Table 3). Thin-section studies reveal that many of the amphibole-rich samples with Zr, Y and Hf enrichments correspond to samples with a high abundance of euhedral zircon crystals and prismatic apatite that are localized in narrow zones and in some cases show high-strain deformation. The origin of apatite and zircon in these rocks is unclear, as many of the original protolith textures have been obliterated by subsequent metasomatism. However, in some cases (e.g., 3646-1205 and 3647-1359), zircon and apatite occur in samples with textures reminiscent of plagioclase-impregnated dunites or troctolites, which contain relict chromium spinels and may be similar to troctolites recovered in the IODP Hole U1309 drillcore [*Expedition Scientific*

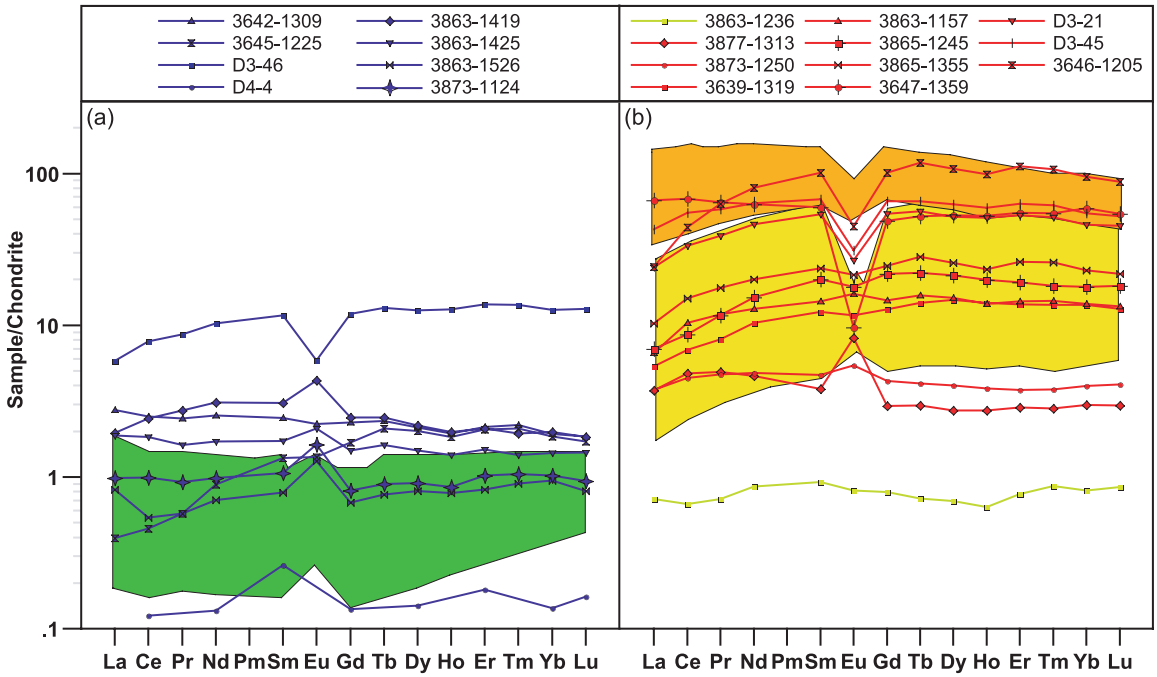

Figure 11. (a) Chondrite-normalized REE concentration patterns of the AM talc schists [after *McDonough and Sun*, 1995]. Green shaded areas show range of compositions of AM serpentinites. Talc-rich rocks show an overall REE enrichment compared to the AM serpentinites. The REE pattern of sample D3-46 is presumably related to melt impregnation. By contrast, the very low REE concentrations of sample D4-4, a talc fels (almost monomineralic talc-rich rock), is presumably related to the abundance of talc, which takes up minimal quantities of REE in its crystal lattice [e.g., *Gillis et al.*, 1992]. (b) Chondrite-normalized REE concentration patterns of amphibole-rich rocks [after *McDonough and Sun*, 1995]. Yellow shaded area shows the range of compositions of the AM gabbroic rocks and orange shaded area shows range of AM oxide gabbros; green line (with square) corresponds to an example of chlorite-rich sample. The REEs define three groups: (1) two samples (3877-1313 and 3873-1250) with lowest REE concentration, positive Eu anomalies (similar to the talc-rich rocks) and petrographic and geochemical evidence for a ultramafic protolith; (2) four samples overlapping the REE compositional range of gabbros; and (3) samples with highest REE concentrations and a strong negative Eu anomaly, resembling Fe-Ti gabbro patterns.

Party, 2005a, 2005b]. The close correlation between the anomalous mineralogies, textures and bulk rock chemistries suggest that the samples with enrichments in Zr, Y, and Hf mark zones of late evolved gabbroic melts that intruded the upper mantle sequences and were subsequently sites of extensive metasomatic overprinting and mass transfer (discussed in detail below).

[53] Chondrite-normalized REE patterns of the two groups differ substantially. The talc-rich samples have a narrow range of REE contents and chondrite-normalized profiles (Figure 11a). The REE content typically range from ~0.1 to 3 times the chondrite-normalized value for light and heavy REE. Sample D3-46, characterized by high Zr, Y and Hf concentrations (discussed above), is an exception and shows an enriched REE pattern (more than 10x chondrite) that overlaps the amphibole-rich sample range (Figure 11b). The talc-rich samples are depleted in light REE or show nearly flat REE patterns. The smooth REE patterns are characterized by slightly positive Eu anomalies (average value of [Eu/Eu*] = 1.36, excluding sample D3-46 ([Eu/Eu*] = 0.50); see footnote in Table 3 for the definition of [Eu/Eu*]).

[54] The amphibole-rich samples define a broad range of REE compositions and show correlations with Zr content (Figure 11b, Table 5). The Zr-rich samples have the highest REE enrichment, while the Zr-poor samples show the lowest concentrations. Accessory minerals such as zircon are known to fractionate many trace elements and high field-strength elements from fluids [*Heaman et al.*, 1990]. The REE content of the Zr-rich samples in this group typically show ~10 to 100 times chondrite-normalized values for light and heavy REE, respectively. In contrast, the Zr-poor samples have ~1 to 10 times the chondrite-normalized light and heavy REE compositions. Most of the samples are LREE-depleted with flat heavy REE patterns. All

Table 5. Bulk Rock Major-Element (wt.%) and Trace-Element (ppm) Compositions of Amphibole-Rich and Chlorite-Rich Metasomatic Rocks

Sample	D3-45	3646-1205	3865-1355	3873-1250	3865-1245	3863-1157	D3-21	3647-1359	3877-1313	3863-1236
Depth, m		2327	783	956	795	862		1623	1009	837
Type	Amph schist	Amph schist	Amph schist	Amph-talc schist	Amph-chl schist	Amph fels	Amph fels	Amph-talc fels	Amph-chl fels	Chlorite-rich
Major Elements, weight %										
SiO_2	43.87	49.69	46.85	44.25	49.41	51.30	49.30	50.84	54.95	28.22
TiO_2	1.155	0.293	1.167	0.310	1.780	0.342	0.402	0.160	<d.l.	0.967
Al_2O_3	7.95	5.69	9.54	10.11	5.15	5.43	4.87	4.50	1.85	20.70
Fe_2O_3	13.95	8.43	5.82	5.35	5.91	4.96	9.08	8.61	3.64	4.94
MnO	0.153	0.163	0.081	0.070	0.120	0.082	0.098	0.141	0.080	0.025
MgO	21.80	24.22	20.67	26.64	22.20	21.99	27.21	26.48	23.34	31.26
CaO	4.55	6.24	11.29	6.44	10.31	11.64	2.65	2.68	12.30	0.11
Na_2O	0.35	0.44	1.98	0.75	0.77	1.59	0.29	0.21	0.50	0.09
K_2O	0.10	<d.l.	0.05	<d.l.	<d.l.	0.06	0.01	0.03	<d.l.	0.02
P_2O_5	0.24	0.01	0.01	0.06	0.15	0.02	0.19	0.08	<d.l.	0.02
LOI*	5.45	4.59	2.74	6.38	3.72	2.15	5.85	5.29	2.98	12.32
Total	99.56	99.78	100.19	100.36	99.52	99.56	99.96	99.41	99.64	98.68
CO_2, wt%	0.21	0.01	0.02	0.00	0.01	0.02	0.03	<d.l.	0.31	0.02
Density, g/cm^3				2.80	2.84		2.80	2.89		
Trace Elements, ppm										
V	118	42	394	113	284	252	40	44	42	573
Cr	633	1390	2590	597	1503	1620	1430	1473	2987	111
Co	69	55	38	65	42	35	59	62	32	52
Ni	572	842	646	1337	854	749	1100	1076	710	1110
Cu	<d.l.	38	<d.l.	<d.l.	<d.l.	<d.l.	<d.l.	<d.l.	<d.l.	<d.l.
Zn	<d.l.	72	<d.l.	<d.l.	31	<d.l.	37	39	32	<d.l.
Ga	16	14	11	12	9	8	9		4	8
Rb	<d.l.	<d.l.	<d.l.	<d.l.	<d.l.	<d.l.	<d.l.	1	<d.l.	<d.l.
Sr	4	5	14	7	8	7	6	5	7	4
Y	79.4	153.2	34.4	5.9	29.8	17.2	66.8	84.0	4.1	1.0
Zr	168	326	67	11	43	4	252	60	<d.l.	<d.l.
Nb	4.2	3.8	1.7	0.9	1.4	0.7	2.3	5.3	0.2	1.3
Cs	<d.l.	<d.l.	<d.l.			<d.l.	<d.l.	<d.l.		<d.l.
Ba	<d.l.	<d.l.	<d.l.	<d.l.	<d.l.	<d.l.	<d.l.	8	<d.l.	<d.l.
La	10.18	5.77	2.44	0.89	1.65	1.56	5.71	15.78	0.88	0.17
Ce	33.69	27.11	9.19	2.76	5.32	6.33	20.53	41.64	2.94	0.41
Pr	5.37	5.85	1.64	0.44	1.08	1.09	3.60	5.99	0.46	0.07
Nd	29.19	36.75	9.18	2.22	6.98	5.86	21.13	28.61	2.12	0.39
Sm	10.03	14.95	3.51	0.70	2.96	2.12	7.94	8.84	0.56	0.14
Eu	1.762	2.529	1.213	0.306	1.010	0.907	1.511	0.546	0.466	0.046
Gd	13.06	20.19	4.90	0.85	4.35	2.90	10.80	9.71	0.59	0.16
Tb	2.37	4.25	1.02	0.15	0.80	0.57	2.03	1.89	0.11	0.03
Dy	15.40	26.46	6.33	0.99	5.25	3.73	12.80	13.01	0.68	0.17

Table 5. (continued)

Sample	D3-45	3646-1205	3865-1355	3873-1250	3865-1245	3863-1157	D3-21	3647-1359	3877-1313	3863-1236
Depth, m		2327	783	956	795	862		1623	1009	837
Type	Amph schist	Amph schist	Amph schist	Amph-talc schist	Amph-chl schist	Amph fels	Amph fels	Amph-talc fels	Amph-chl fels	Chlorite-rich
Ho	3.25	5.41	1.28	0.21	1.09	0.76	2.78	2.88	0.15	0.03
Er	10.14	17.89	4.19	0.60	3.07	2.30	8.49	8.82	0.46	0.12
Tm	1.525	2.627	0.644	0.093	0.449	0.357	1.273	1.351	0.070	0.022
Yb	8.81	15.36	3.72	0.64	2.89	2.23	7.41	9.48	0.48	0.13
Lu	1.286	2.166	0.536	0.100	0.447	0.327	1.109	1.338	0.073	0.021
Hf	5.9	10.4	2.3	0.3	1.3	0.3	7.6	2.6	0.1	0.9
Ta	0.18	<d.l.	0.01	0.05	0.13	<d.l.	0.06	0.40	0.01	<d.l.
Pb	<d.l.	<d.l.	<d.l.			<d.l.	<d.l.	<d.l.		<d.l.
Th	0.26	0.33	0.07	0.06	<d.l.	<d.l.	0.20	1.23	0.06	<d.l.
U	0.09	0.33	0.03	0.03	0.03	<d.l.	0.08	0.29	0.06	0.03
$[La/Yb]_N$	0.79	0.25	0.45	0.94	0.39	0.47	0.52	1.13	1.25	0.88
Eu/Eu*	0.47	0.44	0.89	1.21	0.86	1.11	0.50	0.18	2.45	0.94
$[La/Sm]_N$	0.63	0.24	0.43	0.80	0.35	0.46	0.45	1.11	0.98	0.77
$[Gd/Yb]_N$	1.20	1.06	1.07	1.08	1.22	1.05	1.18	0.83	0.99	0.98
$[Dy/Er]_N$	0.99	0.96	0.98	1.07	1.11	1.05	0.98	0.96	0.96	0.90

of the Zr-rich samples show a negative Eu anomalies (average [Eu/Eu*] value = 0.61), in contrast to the Zr-poor samples with an average [Eu/Eu*] value of 1.51.

[55] Compared to the non-metasomatic protoliths, the talc-rich rocks in general show a slight enrichment in REE relative to the serpentinites but are strongly depleted in these elements relative to the gabbros (Figure 11a). In contrast, the amphibole-rich metasomatic rocks are strongly REE-enriched with respect to the serpentinite but have similar or enriched patterns compared to the gabbros (Figure 11b). The Zr-poor samples show no enrichment with respect to the gabbros, whereas the Zr-rich samples are particularly enriched and lie within the upper range defined by the Fe-Ti oxide-bearing gabbros (Figure 11b).

5. Discussion

5.1. Focused Fluid Flow in High-Strain Domains

[56] Assemblages of talc, calcic amphibole and chlorite are common in hydrothermally metamorphosed oceanic rocks and generally form at a broad range of temperatures under greenschist-facies conditions as replacement of primary or secondary mafic minerals during multistage water/rock interaction or as direct precipitation (in particular talc) upon mixing between hydrothermal fluids and seawater [e.g., *Miyashiro et al.*, 1979; *Hajash and Chandler*, 1981; *Talbi et al.*, 1999; *Escartín et al.*, 2003; *Bach et al.*, 2004; *D'Orazio et al.*, 2004]. Calculations of equilibrium activity diagrams for the system HCl-H_2O-SiO_2-MgO-Al_2O_3 at 150–300°C and 5–86 bars [*Bowers et al.*, 1984] show that, at low Al activities, the stability field of talc lies between that of serpentine and quartz. The lower stability limit ranges from as low as ~310°C for highly aqueous fluids at 1 kbar, to as high as 670°C if the fluid is very H_2O-rich (see *Johannes* [1969] for detailed reaction curves). The mineral assemblage tremolite-chlorite is relatively insensitive to pressure and temperature and may record conditions ranging from greenschist- to upper amphibolite-facies; whereas tremolite-actinolite formation is generally attributed to temperatures of <500°C [*Miyashiro*, 1973]. Serpentine minerals provide the best limit on temperature for the dominant serpentine-bearing assemblages at the Atlantis Massif and indicate greenschist-facies conditions below approximately 425°C [*Evans and Trommsdorff*, 1970; *O'Hanley*, 1996; *Früh-Green*

et al., 2004]. Similar temperatures of metasomatism are indicated by the fact that the talc-tremolite-chlorite assemblages commonly overprint serpentine in the AM basement and fault rocks.

[57] The formation of Ca-amphibole fault rocks or talc metasomatic peridotites is commonly related to tectonic uplift and exposure of atypical sections of the oceanic lithosphere. These rocks have been documented in oceanic core complexes, in fracture zone settings and in other areas where ultramafic rocks are exposed on the seafloor [e.g., *Taylor and Huchon*, 2002; *Escartín et al.*, 2003; *Bach et al.*, 2004; *D'Orazio et al.*, 2004], in ophiolite sequences [e.g., *Miller*, 1988], and in subduction zones [e.g., *King et al.*, 2003]. Talc-rich rocks are frequently recovered with undeformed serpentinite and gabbros, mylonitic gabbros, dikes, plagioclase-impregnated ultramafic rocks, diabases, monomineralic chlorite-rich rocks and minor basalt. This heterogeneous suite of rocks is not representative of the lithologies typically found in stratiform ophiolites sequences [*Penrose Conference Participants*, 1972; *Moores et al.*, 1984] and therefore probably represents the locus of thermal, mechanical and fluid processes that are not typically developed during seafloor spreading. Outcrop relationships integrated with petrography and geochemistry of samples from the Atlantis Massif show a dominance of undeformed over deformed rocks, reflecting the fact that high-strain deformation is highly localized along the detachment shear zone, leaving a large portion of the exposed lithosphere undeformed.

[58] Infiltrating metasomatic fluids during low- to medium-grade metamorphism play an important role in the evolution of these shear zones. In particular, fault weakening would be a consequence of the development of talc-amphibole-chlorite-serpentine gouge mineralogies. The resulting strain localization would result in enhanced hydrothermal fluid migration within the permeable, porous, and anisotropic fault zone and possibly lead to elevated fluid pressures [*Escartín et al.*, 2003]. Large gradients in fluid pressure and permeability may result, and they in turn may lead to continued, focused fluid flow. Focusing of fluid flow along relatively narrow, structurally weakened domains explains why syn-mylonitic retrogression is more pervasive in zones of high shear strain than in the less deformed wall rocks, even though all lower-plate rocks undergo the same drop in pressure and temperature as they are uplifted [*Reynolds and Lister*, 1987].

[59] *Schroeder and John* [2004] demonstrate that the structural evolution of the Atlantis Massif is broadly similar to that of continental metamorphic core complexes and that the resulting core complex dome and detachment fault geometry are similar to many other oceanic core complexes. They present important microstructural and mineralogical evidence for progressive deformation from granulite to sub-greenschist facies conditions and conclude that the gabbroic rocks were only weakly deformed below amphibolite-facies conditions (<500 C), with strain being partitioned into the altered peridotite at low temperature. On the basis of detailed analyses of a limited number of samples from the shear zone, *Schroeder and John* [2004] argue that semibrittle strain is localized into a zone <100 m beneath the main detachment surface and that brittle strain (based primarily on sample 3652-1309) is restricted to <10 m beneath the detachment.

[60] Our results are consistent with the studies by *Schroeder and John* [2004], which show that an earlier phase of high-temperature, hydrous crystal plastic deformation is particularly well preserved in the gabbroic rocks and that the peridotites are affected by pervasive serpentinization. However, our studies do not substantiate the presence of a narrow brittle zone at the top of the massif nor the partitioning of strain solely into peridotites. Our detailed mapping and a higher density of sampling at the top of the southern wall allow us to identify the detachment fault zone [*Kelley et al.*, 2005; Karson et al., submitted manuscript, 2005]. Our results indicate that this zone cuts a domain of serpentinites that had been intruded by gabbroic rocks, both of which underwent a similar alteration and deformation history but record heterogeneous deformation under greenschist-facies conditions. The earlier, high-temperature deformation zones served as permeable zones for subsequent localized fluid flow and lower temperature, greenschist-facies alteration and metasomatism. Thus the metasomatic rocks mark the zone of detachment faulting in the southern part of the AM and provide evidence of channeled fluid flow and mass transfer during the long-lived detachment history (Figure 12). This zone can be traced for several kilometers along strike, but is <100 m thick, implying strong localization of strain (Karson et al., submitted manuscript, 2005) with little or no strain accommodated by the host rock below the shear zone. Outcrop observations and petrological analyses indicate that deformation associated with the later talc-amphibole

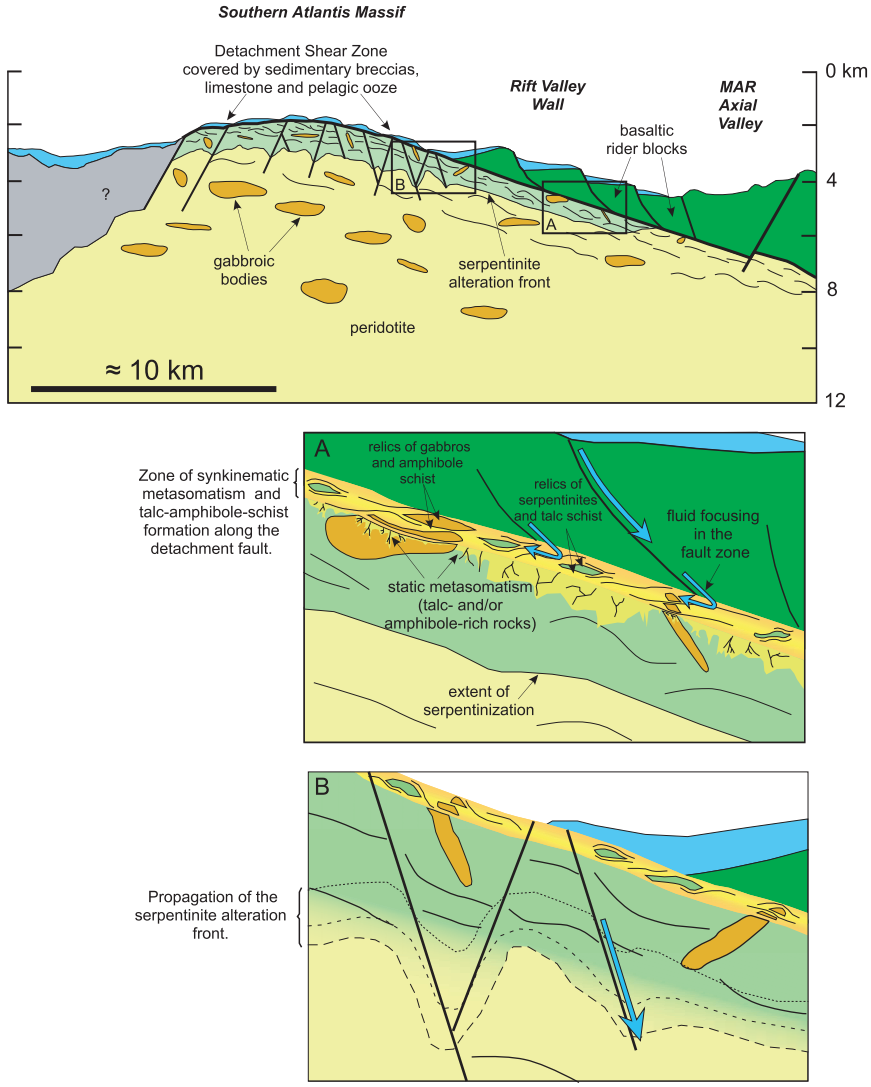

Figure 12. Interpretative cross section of the Atlantis Massif (no vertical exaggeration), with detailed areas showing fluid pathways, metasomatic zones, and extent of serpentinization (light green shaded region) related to detachment faulting and steep normal faults (modified from Karson et al. (submitted manuscript, 2005)). Box A: detail of the narrow shear zone (<100 m) along the detachment surface (in red-yellow) characterized by heterogeneous, variably altered and deformed gabbroic and peridotite lithologies and with extensive synkinematic metasomatism. Fluids were focused along the detachment and through discrete ductile shear zones triggering metasomatism of serpentinites and gabbros. The resulting talc-amphibole schists enclose lenses of relic, locally less deformed serpentinite and gabbroic rocks. The footwall was affected by a diffuse and static metasomatism mainly driven by a cataclastic network of fractures. Box B: detail showing widespread ongoing serpentinization related to a complex network of steeply dipping faults that enhance penetration of seawater into relatively cool, fresh peridotite, promote propagation of the serpentinization front, and ultimately lead to the formation of the LCHF.

assemblages under greenschist-facies conditions is highly heterogeneous and is marked by crystal-plastic (talc- and/or amphibole-schist) to cataclastic (talc-amphibole fels or talc-amphibole serpentinites) behavior.

[61] We conclude that the mineral assemblages and microstructures in the AM basement rocks indicate multiple phases of high strain deformation and that deformation and fluid flow was often focused in the same limited band of rocks over a wide range of temperatures and fluid compositions (Figure 12). In contrast, microfracturing affected the surrounding areas and is characterized by the presence of talc-amphibole fels cut by networks of veins and veinlets, which have led to a more pervasive, predominantly static metasomatism that affected a larger portion

of the wallrocks (e.g., Figures 4b, 6c, and 6f). This relationship suggests that a significant amount of metasomatism was controlled by diffuse fluid flow and mass transfer associated with fractures that lack a strong preferred orientation.

[62] Deformation along detachment shear zones is intimately connected to the tectonic evolution of the core complex and to the evolving geometry of the shear zone. A number of structural and tectonic studies interpret detachment faults as cutting the entire thickness of the lithosphere and soling-out at the brittle-plastic transition [*Tucholke et al.*, 1998, 2001], at a melt-rich hot zone near the gabbro-dike transition [*Dick et al.*, 1991], or along an alteration front horizon at relatively shallow depth within the brittle lithosphere [*MacLeod et al.*, 2002; *Escartín et al.*, 2003]. According to evolving-shear-zone models across the brittle-plastic transition [*Tucholke et al.*, 1998, 2001], detachment faulting and associated brittle deformation occur in the upper levels of a detachment fault zone, but grade down-dip into a zone of crystal-plastic deformation dominated by mylonites [*Reynolds and Lister*, 1987]. However, in some cases, such as at the MAR 15°45′N OCC, high-temperature metamorphism and deformation of the footwall may be minimal and detachment faulting may be localized along brittle deformation zones in relatively cold serpentinized mantle peridotites [*MacLeod et al.*, 2002; *Escartín et al.*, 2003]. The preservation of granulite- to amphibolite-facies deformation fabrics and the predominance of crystal-plastic deformation under greenschist-facies conditions in the southern part of the Atlantis Massif is distinct from the relatively restricted deformation recorded in the IODP Hole U1309 core [*Expedition Scientific Party*, 2005a, 2005b] and contrasts with the mainly cataclastic, greenschist-facies deformation observed in talc-rich zones recovered from the MAR 15°45′N core complex [*Escartín et al.*, 2003]. This difference likely reflects the fact that detachment faults can have different strain rates and can cut and expose different structural levels of the oceanic lithosphere during the long-lived evolution of an OCC [*Escartín et al.*, 2003]. However, the dominance of similar talc-amphibole mineral assemblages at 15°45′N is similar to the southern AM and provides further evidence for the importance of detachment fault zones in channeling seawater-dominated fluids within lithologically heterogeneous sections of the lower crust and upper mantle sections of the lithosphere and promoting mass transfer and metasomatism during exhumation of gabbro-peridotite massifs.

5.2. Mass Transfer During Oceanic Detachment Faulting

[63] The mineralogy and chemistry of altered rocks recovered from the seafloor reflect the integrated effects of multistage magmatic/hydrothermal processes and provide a record of the extent of chemical exchange between the crust and seawater, the nature of the reactions that have taken place, and variations in the composition of the circulating fluids. Direct sampling of fluids [e.g., *Kelley et al.*, 2001, 2005; *Douville et al.*, 2002], thermodynamic modeling [e.g., *Wetzel and Shock*, 2000; *Palandri and Reed*, 2004], and experiments [*Hajash and Chandler*, 1981; *Janecky and Seyfried*, 1986; *Allen and Seyfried*, 2003] indicate that hydrothermal fluids in ultramafic- and mafic-hosted hydrothermal systems are depleted in Mg and enriched in SiO_2 with respect to seawater. Experimental studies of *Allen and Seyfried* [2003] indicate that alteration of pyroxenes during harzburgite-seawater interaction at 400°C provides an important source of silica. However, *Wetzel and Shock* [2000] have shown that, at 350°C and 500 bars, mafic rock-seawater reactions form hydrothermal fluids that are orders of magnitude higher in silica and lower in pH than hydrothermal fluids produced by reaction of seawater with ultramafic rocks. Interaction with such Si-rich fluids can thus lead to talc formation in the neighboring serpentinites, as is observed in serpentinites drilled at ODP Site 1268 [*Bach et al.*, 2004].

[64] Despite differences in deformation, the ubiquitous occurrence of talc, amphibole, and chlorite associated with different protoliths in the fault zone at the AM suggests a common origin of the metasomatic fluid. The chemistries and microfabrics indicate that the hydrothermal fluid responsible for the retrograde, disequilibrium assemblages must have been relatively cool ($\leq$500°C), oxidizing, and Si-Al-Ca-rich, and was likely derived by interaction with the gabbroic rocks. Our petrological, bulk rock geochemical and isotopic data [*Delacour et al.*, 2004] strongly support the interpretation that the amphibole-rich fault rocks are sites of metasomatic gabbro-seawater interaction and that the talc-rich fault rocks are domains in which gabbro-derived, oxidizing Si-rich fluids interacted with the serpentinites. The relatively high Ni and Cr concentrations in the amphibole-rich rocks (Figure 10) could reflect mixed ultra-

mafic/gabbroic precursor domains or local mass transfer from the serpentinite to the mafic rocks during alteration. Metasomatic interaction between gabbroic and peridotite rocks is further evident by the close association with monomineralic chlorite-rich rocks and rodingite, characteristic of a blackwall reaction zones in some ophiolite complexes [*Frost*, 1975; *Evans*, 1977] and indicative of infiltration metasomatism associated with ultramafic rocks. Thus the metasomatic rocks within the detachment fault zone at the AM most likely mark the contacts between gabbroic and ultramafic lithologies and zones of channeled fluid flow, in which the resulting hydrous mineral assemblages provided nucleation sites for slip and localization of high-strain deformation (Figure 12).

[65] The AM fault rocks display progressive metasomatic alteration from partially serpentinized peridotite to talc-amphibole-rich rocks, and from gabbroic rocks, pyroxenitic body and/or impregnated peridotite to amphibole-rich rocks. The talc-rich fault rocks have clear petrographic relationships with the serpentinite protoliths and have trace element (e.g., Cr and Ni) compositions indicative of precursory peridotite. However, they show marked changes in their major element compositions (Figure 9) and are slightly enriched in REE compared to the serpentinite protoliths. In addition, the AM talc-amphibole serpentinites contain an average of 6.7 wt% LOI (predominantly as H_2O) compared to 13.1 wt% in the serpentinites and indicate that the serpentinite protoliths have undergone dehydration to form talc-rich assemblages. The change in LOI reflects an important aspect of the talc-in reaction, in that approximately half of the structurally bound water in the system is remobilized.

[66] The amphibole-rich fault rocks have a composite appearance and suggest more complex and heterogeneous protoliths. Major and minor element abundances indicate that most of the samples presently have mafic compositions and may be gabbroic in origin. A strong enrichment in incompatible elements such as Zr, Y and Hf are characteristic of many samples analyzed in our study; however, their origin remains controversial. High field strength elements (HFSE; e.g., Zr, Hf, Nb, and Ta) have previously been thought to be immobile during metamorphism [e.g., *Floyd and Winchester*, 1978; *Corfu and Davis*, 1991]. However, recent studies have shown that such elements are, in some circumstances, mobile in hydrothermal systems [*Nesbitt et al.*, 1999; *Gieré*, 1990; *Rubin et al.*, 1993; *King et al.*, 2003; *Allen and Seyfried*, 2005] and the higher concentrations of Zr, Hf, Nb, and Ta could reflect mobility of the HFSE during fluid/rock interaction at depth (i.e., via the breakdown of silicates and heavy minerals). Acidic, F- and Cl-bearing aqueous fluids are regarded as important carriers of Zr in hydrothermal systems; phosphate, sulfate, and carbonate anions are also suggested as ligands for Zr complexing [*Dubinska et al.*, 2004]. Recently, *Dubinska et al.* [2004] reported occurrences of hydrothermal zircon from rodingite blackwall assemblages from the Jordanòw–Gogolòw serpentinite massif. They suggest that zircon co-precipitated with corrensite and chlorite from low-temperature (270–300°C), alkaline fluids genetically related to serpentinization. The zircon crystallization in the blackwall was possibly due to a local pH decrease in microdomains related to fixing of OH- by chlorite and corrensite [*Dubinska et al.*, 2004].

[67] Alternatively, it is possible that the AM fault rocks enriched in these elements are derived from protoliths with higher modal amounts zircon and apatite, or are the product of interaction between a mafic or ultramafic protolith with late evolved melt. Similarly, peridotite sample 209-1270D-3R-1 from ODP Site 1270 (Leg 209 [*Kelemen et al.*, 2004]) is intruded by a gabbroic dikelet, and displays significantly higher incompatible element contents (20 ppm Y and 96 ppm Zr), suggesting that the parent melt to the veins was enriched in highly incompatible trace elements or perhaps these veins crystallized from liquids extracted from evolved gabbronorites.

[68] The lack of preserved preliminary minerals and textures makes it difficult to unravel the effects of mixed lithologies and mass transfer by melts and fluids, thus the significance of the high concentrations of Zr, Y and Hf in the amphibole-rich rocks remains equivocal. However, at the southern Atlantis Massif, most of the Fe-Ti oxide-gabbros, a few of the gabbros, and a small number of peridotites containing metasomatic assemblages in veins show similar enrichments (Table 3). Comparable zones of oxide gabbros enriched in apatite and zircon as accessory minerals were recovered in the IODP Hole U1309 core [*Expedition Scientific Party*, 2005b]. The correlation between high zircon and apatite contents and the presence of zones of evolved melts (e.g., oxide gabbros) is characteristic of lower crustal sequences in many slow- and ultra-slow spreading environments [e.g., *Dick et al.*, 1999]; in the MARK area [*Karson et al.*,

1997]; and at 15°N at the MAR [*Kelemen et al.*, 2004]. Our petrological observations and geochemical data are thus consistent with an interpretation that these enrichments in the AM fault rocks are likely related to the presence of precursory zones of evolved melt in the mafic or ultramafic rocks that underwent subsequent metasomatism during the development of the DSZ.

[69] The AM amphibole-rich fault rocks show no significant depletion in REE concentration with respect to the gabbroic rocks. In contrast, the talc-rich fault rocks have enriched REE patterns relative to the serpentinites (Figure 11) that are intermediate between the serpentinite and gabbro compositions. This relationship suggests that metasomatic gabbro-seawater interaction may have produced REE-enriched fluids that interacted with the serpentinites to produce the talc-rich rocks. It is generally accepted that the mobility of REE is limited during hydrothermal alteration of mafic rock [*Humphris and Thompson*, 1978; *Gillis et al.*, 1992]. Moreover, the facts that REE patterns of vent fluids are uniform, are enriched compared to seawater [*Elderfield and Greaves*, 1982], and resemble those of plagioclase have been inferred to indicate control of the REE contents in the fluids by plagioclase at high fluid-rock ratios [*Klinkhammer et al.*, 1994; *Douville et al.*, 1999]. Other processes, such as REE complexation by ligands (Cl^-, F^-, SO_4^{2-}), secondary interstitial phase precipitation, and phase separation can enhance REE mobility and modify REE distributions in deep-sea hydrothermal fluids [*Bach and Irber*, 1998; *Douville et al.*, 2002; *Allen and Seyfried*, 2005]. However, hydrothermal alteration of a rock typically will not result in appreciable changes to its REE bulk composition, unless the protolith contains primary or secondary phases that are unusually reactive [*Allen and Seyfried*, 2005].

[70] An interpretation that the REE enrichment in the AM talc schist resulted from gabbro-seawater interaction is consistent with recent experiments by *Allen and Seyfried* [2005], who conclude that chondrite-normalized REE patterns are influenced greatly by fluid speciation effects and secondary mineral formation processes. Because the REE concentrations of seawater are nearly 1000 times lower than in the gabbroic rocks, very little change in the overall abundance of REE in the gabbro during seawater-rock interaction would be needed to account for relatively large changes in concentration of REE in the resulting hydrothermal fluid [see also *Allen and Seyfried*, 2005]. This enrichment may be attributed to REE uptake in the secondary mineral phases in the talc-rich rocks. Although phyllosilicates, such as chlorite, talc, and serpentine, do not take up large quantities of REE in their crystal lattice [e.g., *Gillis et al.*, 1992], amphiboles can incorporate significant amounts of REE at hydrothermal temperatures [e.g., *Gillis and Meyer*, 2001] (Figure 11). Thus the enriched REE contents of the talc-rich rocks could be controlled by varying amounts of amphibole. Alternatively, REE may be concentrated along the grain boundaries of secondary minerals during recrystallization [*Bach and Irber*, 1998].

[71] The serpentinized peridotites at the Atlantis Massif have characteristically high U contents compared to unaltered peridotite compositions. In contrast, all of the AM metasomatic fault rocks have lower contents of U compared to the serpentinite protoliths but higher contents compared to the gabbros. Seawater is characterized by extremely low REE contents ($\sim 10^{-7}$–10^{-6} ppm by weight), by negative Ce and Eu anomalies, and by U contents of ~3.2 ppb [*Holland*, 1978; *Elderfield and Greaves*, 1982; *Chen et al.*, 1986]. In contrast, reduced submarine hydrothermal fluids usually exhibit strong depletions in U concentrations relative to seawater [e.g., *Michard et al.*, 1983; *Chen et al.*, 1986] and reflect uranium uptake in the rocks. The elevated U concentrations of the AM metasomatic rocks relative to unaltered gabbroic and peridotite compositions substantiate our interpretation that the metasomatic fluid was originally seawater and was strongly modified during fluid-rock interaction. In addition, the variations in bulk rock chemistry of the AM fault rocks most likely reflect heterogeneous fluid compositions during serpentinization and metasomatism, and the characteristically high U contents of the serpentinites suggests preferential uptake of uranium during serpentinization or higher fluid fluxes in the peridotite-dominated domains of the Atlantis Massif.

6. Conclusions

[72] The integrated field, petrological and geochemical study of mafic and ultramafic rocks exposed on the south wall of the Atlantis Massif provides new insights into how major detachment shear zones evolve during the development of OCCs and demonstrates the interplay of fluids, mass transfer, and metamorphism in strain locali-

zation associated with this process. For the first time a major, subhorizontal detachment shear zone could be mapped for at least 3 km along the top edge of an OCC (Karson et al., submitted manuscript, 2005). Detailed sampling within this well-constrained geological context provides unprecedented outcrop-scale constraints on the distribution, the deformation, and the metamorphism of the basement rocks in the footwall of the massif relative to the detachment shear zone.

[73] Our results indicate that metasomatic fault rocks recovered from the DSZ of the southern Atlantis Massif are key elements of this OCC and record a deformation and metamorphic history that is distinct from the underlying basement rocks. The talc-amphibole-chlorite-mineral assemblages and microstructures in the fault rocks indicate multiple phases of fluid infiltration and high strain deformation in limited domains. In a number of samples we find evidence that pre-existing, high-temperature deformation zones served as permeable zones for subsequent localized fluid flow and lower temperature, greenschist-facies alteration and metasomatism (Figure 12). Whereas the metagabbroic rocks are important in revealing the early high-temperature, hydrous metamorphic and deformation history of the massif, the underlying peridotites that we sampled are dominated by pervasive, static serpentinization that could only have occurred below temperatures of ~425°C. Along the DSZ, we found only minimal evidence for penetrative cataclastic deformation and sub-greenschist-facies overprinting to chlorite-rich assemblages, as is commonly observed in continental core complexes. Although a limited number of cataclasite samples were recovered during the 2000 cruise close to the top of the massif [*Schroeder and John*, 2004], our broader sampling suggests this is not representative of the DSZ. Viewed from this perspective, the cataclastic deformation, predominately characterized by more diffuse brittle fracturing and static replacement, is focused in less deformed domains in the main shear zone surrounding discrete metasomatic zones or is controlled by fracture-zone related, steep normal faults that extend into structurally deeper basement rocks beneath the shear zone.

[74] The varying mineralogies of the AM metasomatic rocks are characteristic of blackwall assemblages and reflect seawater-rock interaction in a lithologically variable section of the oceanic lithosphere (Figure 12). Our petrological and geochemical data show that the bulk rock and hydrothermal fluid compositions were controlled by the chemical compositions of the protoliths and are independent of the degree of deformation. In this heterogeneous section of the oceanic lithosphere exposed on the south wall of the massif, where gabbroic rocks are volumetrically variable and inter-dispersed with serpentinized peridotites, seawater compositions of the hydrothermal fluid were locally modified by interaction with gabbroic rocks to produce oxidizing, Si-Al-Ca-rich fluids at relatively low temperatures ($\leq$500°C). The formation and the evolution of one or more detachment surfaces promoted focused fluid flow and mass transfer along discrete shear zones (Figure 12). This type of flow was distinct from the more pervasive circulation into the Atlantis Massif that has led to strongly serpentinized domains on the south wall of the massif and which appears to be presently ongoing below the Lost City hydrothermal field. Continuous tectonic uplift, reflected by the bathymetry near the Atlantis Fracture Zone and the presence of steep normal faults cutting the south wall, would have promoted hydrothermal circulation and serpentinization in this particular volume of oceanic lithosphere. Volume increases associated with serpentinization and expansion, as well as mass wasting probably sustains these faults as permeable pathways for hydrothermal flow [*Kelley et al.*, 2005; Karson et al., submitted manuscript, 2005].

[75] Dehydration of serpentinite to talc- and amphibole-rich assemblages occurring simultaneously with deformation can produce weakening by different mechanisms that are not exclusive of each other. Moreover the production of talc, a distinctly mechanically weak phase [*Escartín et al.*, 2004], facilitates the dislocation along the detachment and lowers the shear strength. *MacLeod et al.* [2002] have suggested that strain localization along the fault plane near the Fifteen-Twenty Fracture Zone of the MAR was highly effective and long-lived, almost certainly as a result of the presence of very weak minerals such as serpentine, talc, and other silicates (i.e., chlorite, tremolite). While we have gained significant knowledge on the rheological and mechanical proprieties of some of the lithospheric components such as olivine, dolerite and serpentinite [*Escartín et al.*, 1997; *Moore et al.*, 1997], our knowledge of the role of fluids (water, melt) or the significance of compositional variations of other important alteration products, such as talc, amphibole and chlorite, remains limited. *Escartín et al.* [2004] reported experiments to characterize the mechanical behavior of talc

and show that the presence of even small amounts of talc can substantially weaken the volumes of rock, affecting its behavior and evolution of shear zones. Furthermore, *Tenthorey and Cox* [2003] presented experiments of the permeability evolution of an actively dehydrating serpentinite and showed that dehydration of serpentinite leads to a large transitory increase in porosity and permeability, an observation that has important implications for naturally dehydrating systems in subducting slabs and in middle- to lower-crustal metamorphic regimes.

[76] Our results highlight the potential importance of complex mineral parageneses and fluid-rock interaction that may play a major role in determining the rheology of focused alteration of lower crust and upper mantle along detachment shear zones in OCCs. As discussed above, the complex inter-relationships between tectonic and hydrothermal activity revealed at the south wall of the Atlantis Massif contrast greatly with the results of IODP drilling in the central massif, 5 km to the north. In particular, the rocks recovered from Hole U1309D show minimal talc-amphibole metasomatism, little deformation, and a distinct absence of amphibolite-facies alteration and deformation, suggesting that large-scale deformation and metasomatism associated with a detachment fault was either not recovered in the upper section of the core at Site U1309 or occurred at low temperature [*Expedition Scientific Party*, 2005b]. Although drilling in the central portion of the massif recovered little evidence for distinct zones of metasomatism, the results are consistent with the low-temperature shallow detachment fault model proposed by *MacLeod et al.* [2002] and *Escartín et al.* [2003] for the MAR 15°45′N OCC. The distinct differences in lithologies, metamorphic overprinting and degree of deformation demonstrates the extensive, complex lateral and vertical heterogeneity in composition, alteration, and structure of this OCC, and reflects the fact that different structural levels of the oceanic lithosphere are exposed during the long-lived evolution of an OCC [*Escartín et al.*, 2003; *Expedition Scientific Party*, 2005b]. The distinct differences in lithologies and sharp change in topography from the south wall to the central dome further suggests that normal faults and volume changes may have been significant in the uplift and emplacement of this portion of the Atlantis Massif. These results further highlight the need for comprehensive studies of OCCs and the fact that a single fault model may not be sufficient to understand the complexities in magmatic, tectonic and metamorphism that affect and expose many of the gabbro-peridotite massifs in slow- and ultra-slow spreading environments.

Acknowledgments

[77] We thank the captains, crews, and technical staff aboard R/V *Atlantis* during cruises AT3-60 and AT7-34 to the Atlantis Massif in 2000 and 2003 for their tremendous support of this project. We also acknowledge Donna Blackman and the scientific parties from these cruises for their many contributions to the data collection and discussions at sea. We thank Filippo Olmi, Luca Caricchi, Eric Reusser, and Luigi Burlini for assistance with analyses and Mitch Elend for image processing. Constructive comments by the associate editor, Wolfgang Bach, and an anonymous reviewer greatly improved the paper. This work was supported by ETH grant 0-20890-01 and Swiss SNF grant 2100-068055 to Früh-Green and NSF grants OCE-9712430 and 0136816 to Karson and Kelley.

References

Allen, D. E., and W. E. Seyfried (2003), Compositional controls on vent fluids from ultramafic-hosted hydrothermal systems at midocean ridges: An experimental study at 400°C, 500 bars, *Geochim. Cosmochim. Acta*, *67*, 1531–1542.

Allen, D. E., and W. E. Seyfried (2005), REE controls in ultramafic hosted MOR hydrothermal systems: An experimental study at elevated temperature and pressure, *Geochim. Cosmochim. Acta*, *69*, 675–683.

Bach, W., and W. Irber (1998), Rare earth element mobility in the oceanic lower sheeted dyke complex: Evidence from geochemical data and leaching experiments, *Chem. Geol.*, *151*, 309–326.

Bach, W., C. J. Garrido, H. Paulick, J. Harvey, and M. Rosner (2004), Seawater-peridotite interactions: First insights from ODP Leg 209, MAR 15°N, *Geochem. Geophys. Geosyst.*, *5*, Q09F26, doi:10.1029/2004GC000744.

Bailey, S. W. (1980), Summary of recommendations of AIPEA nomenclature committee, *Clay Miner.*, *15*, 85–93.

Blackman, D. K., J. R. Cann, B. Janssen, and D. K. Smith (1998), Origin of extensional core complexes: Evidence from the Mid-Atlantic Ridge at Atlantis Fracture Zone, *J. Geophys. Res.*, *103*, 21,315–21,333.

Blackman, D. K., et al. (2004), Geology of the Atlantis Massif (Mid-Atlantic Ridge, 30°N): Implications for the evolution of an ultramafic oceanic core complex, *Mar. Geophys. Res.*, *23*, 443–469.

Boschi, C., G. L. Früh-Green, and D. S. Kelley (2003), Links between tectonic and serpentinization processes and their consequences for hydrothermal activity (Atlantis Massif, MAR 30°N) (abstract), *Geophys. Res. Abstr.*, *5*, 09796.

Bowers, T. S., K. J. Jackson, and H. C. Helgeson (1984), *Equilibrium Activity Diagrams for Coexisting Minerals and Aqueous Solutions at Pressures and Temperatures to 5 kb and 600°C*, 397 pp., Springer, New York.

Canales, J. P., B. E. Tucholke, and J. A. Collins (2004), Seismic reflection imaging of an oceanic detachment megamullion (Mid-Atlantic Ridge, 30°10′N), *Earth Planet. Sci. Lett.*, *222*, 543–560.

Cann, J. R., D. K. Blackman, D. K. Smith, E. McAllister, B. Janssen, S. Mello, E. Avgerinos, A. R. Pascoe, and

J. Escartín (1997), Corrugated slip surfaces formed at North Atlantic ridge-transform intersections, *Nature*, *385*, 329–332.

Cannat, M., D. Bideau, and H. Bougault (1992), Serpentinized peridotites and gabbros in the Mid-Atlantic Ridge axial valley at 15°37 N and 16°52 N, *Earth Planet. Sci. Lett.*, *109*, 87–106.

Chen, J. H., Cl. J. Wasserrurg, K. L. Von Damm, and J. M. Edmond (1986), The U-Th-Pb systematics in hot springs on the East Pacific Rise at 21°N and Guaymas Basin, *Geochim. Cosmochim. Acta*, *50*, 2467–2479.

Chidester, A. H. (1962), Petrology and geochemistry of selected talc-bearing ultramafic rocks and adjacent country rocks in north-central Vermont, *U.S. Geol. Surv. Prof. Pap.*, *345*.

Collins, J. A., B. E. Tucholke, and J. Canales (2001), Structure of Mid-Atlantic Ridge megamullions from seismic refraction experiments and multichannel seismic reflection profiling, *Eos Trans. AGU*, *82*(47), Fall Meet. Suppl., Abstract T11C-0865.

Corfu, F., and D. W. Davis (1991), Comment on "Archean hydrothermal zircon in the Abitibi greenstone belt: Constraints on the timing of gold mineralization" by J. C. Claoué-Long, R. W. King, and R. Kerrich, *Earth Planet. Sci. Lett.*, *104*, 545–552.

Crittenden, M. D., P. J. Coney, and G. H. Davis (Eds.) (1980), *Cordilleran Metamorphic Core Complex*, *Mem. Geol. Soc. Am.*, vol. 153, 490 pp., Geol. Soc. of Am., Washington, D. C.

D'Orazio, M., C. Boschi, and D. Brunelli (2004), Talc-rich hydrothermal rocks from the St. Paul and Conrad fracture zones in the Atlantic Ocean, *Eur. J. Mineral.*, *16*, 73–83.

Deer, W. A., R. A. Howie, and J. Zussman (1997), *Rock-Forming Minerals*, vol. 2B 2nd ed., *Double-Chain Silicates*, 764 pp., Geol. Soc., London.

Delacour, A., G. L. Früh-Green, M. Frank, S. M. Bernasconi, C. Boschi, and D. S. Kelley (2004), Fluid-rock interaction in the basement of the Lost City vent field: Insights from stable and radiogenic isotopes, *Eos Trans. AGU*, *85*(47), Fall Meet. Suppl., Abstract B13A-0198.

Dick, H. J. B., H. Schouten, P. S. Meyer, D. G. Gallo, H. Bergh, R. Tyce, P. Patriat, K. Johnson, J. Snow, and A. Fisher (1991), Tectonic evolution of the Atlantis II fracture zone, *Proc. Ocean Drill. Program Sci. Results*, *118*, 359–398.

Dick, H. J. B., et al. (1999), *Proceedings of the Ocean Drilling Program*, *Science Results* [online], vol. 176, Ocean Drill. Program, College Station, Tex. (Available at http://www-odp.tamu.edu/publications/176_SR/176TOC.HTM)

Dick, H. J. B., et al. (2000), A long in situ section of the lower ocean crust: Results of ODP Leg 176 drilling at the Southwest Indian Ridge, *Earth Planet. Sci. Lett.*, *179*, 31–51.

Douville, E., P. Bienvenu, J. Charlou, J. Donval, Y. Fouquet, P. Appriou, and T. Gamo (1999), Ytrium and rare earth elements in fluids from various deep-sea hydrothermal systems, *Geochim. Cosmochim. Acta*, *63*, 627–643.

Douville, E., J. L. Charlou, E. H. Oelkers, P. Bienvenu, C. F. Jove Colon, J. P. Donval, Y. Fouquet, D. Prieur, and P. Appriou (2002), The Rainbow vent fluids (36°14′N, MAR): The influence of ultramafic rocks and phase separation on trace metal content in Mid-Atlantic Ridge hydrothermal fluids, *Chem. Geol.*, *184*, 37–48.

Dubinska, E., P. Bylina, A. Kozlowski, W. Dorr, K. Nejbert, J. Schastok, and C. Kulicki (2004), U-Pb dating of serpentinization: Hydrothermal zircon from a metasomatic rodingite shell (Sudetic ophiolite, SW Poland), *Chem. Geol.*, *203*, 183–203.

Elderfield, H., and M. J. Greaves (1982), The rare earth elements in sea water, *Nature*, *296*, 214–219.

Escartín, J., G. Hirth, and B. Evans (1997), Nondilatant brittle deformation of serpentinites: Implications for Mohr-Coulomb theory and the strength of faults, *J. Geophys. Res.*, *102*(B2), 2897–2913.

Escartín, J., C. Mével, C. J. MacLeod, and A. M. McCaig (2003), Constraints on deformation conditions and the origin of oceanic detachments: The Mid-Atlantic Ridge core complex at 15°45′N, *Geochem. Geophys. Geosyst.*, *4*(8), 1067, doi:10.1029/2002GC000472.

Escartín, J., G. Hirth, and B. Evans (2004), Rheology of talc: Consequences for subduction processes and the localization of deformation, *Eos Trans. AGU*, *85*(47), Fall Meet. Suppl., Abstract S51B-0145.

Evans, B. W. (1977), Metamorphism of alpine peridotite and serpentinite, *Annu. Rev. Earth Planet. Sci.*, *5*, 397–447.

Evans, B. W., and V. Trommsdorff (1970), Regional metamorphism of ultramafic rocks in the Central Alps: Parageneses in the system CaO-MgO-SiO_2–H_2O, *Schweiz. Mineral. Petrogr. Mitt.*, *50*, 481–492.

Expedition Scientific Party (2005a), Oceanic core complex formation, Atlantis Massif, *IODP Prelim. Rep. 304*, Ocean Drill. Program, College Station, Tex. (Available at http://iodp.tamu.edu/publications/PR/304PR/304PR.PDF)

Expedition Scientific Party (2005b), Oceanic core complex formation, Atlantis Massif, *IODP Prelim. Rep.*, *305*, Ocean Drill. Program, College Station, Tex. (Available at http://iodp.tamu.edu/publications/PR/305PR/305PR.PDF)

Floyd, P. A., and J. A. Winchester (1978), Identification and discrimination of altered and metamorphosed volcanic rocks using immobile elements, *Chem. Geol.*, *21*(3–4), 291–306.

Frost, B. R. (1975), Contact metamorphism of serpentinite, chloritic blackwall and rodingite at Paddy-Go-Easy Pass, Central Cascades, Washington, *J. Petrol.*, *16*(2), 272–313.

Früh-Green, G. L., D. S. Kelley, S. M. Bernasconi, J. A. Karson, K. A. Ludwig, D. A. Butterfield, C. Boschi, and G. Proskuroski (2003), 30,000 years of hydrothermal activity at the Lost City vent field, *Science*, *301*, 495–498.

Früh-Green, G. L., J. A. D. Connolly, D. S. Kelley, A. Plas, and B. Grobéty (2004), Serpentinization of oceanic peridotites: Implications for geochemical cycles and biological activity, in *The Subseafloor Biosphere at Mid-Ocean Ridges*, *Geophys. Monogr. Ser.*, vol. 144, edited by W. D. Wilcock et al., pp. 119–136, AGU, Washington, D. C.

Gieré, R. (1990), Hydrothermal mobility of Ti, Zr and REE examples from the Bergell and Adamello contact aureoles (Italy), *Terra Nova*, *2*, 60–67.

Gillis, K. M., and P. S. Meyer (2001), Metasomatism of oceanic gabbros by late stage melts and hydrothermal fluids: Evidence from the rare earth element composition of amphiboles, *Geochem. Geophys. Geosyst.*, *2*(3), doi:10.1029/2000GC000087.

Gillis, K. M., J. N. Ludden, and A. D. Smith (1992), Mobilization of REE during crustal aging in the Troodos Ophiolite, Cyprus, *Chem. Geol.*, *98*, 71–86.

Gillis, K. M., G. Thompson, and D. S. Kelley (1993), A view of the lower crustal component of hydrothermal systems at the Mid-Atlantic Ridge, *J. Geophys. Res.*, *98*, 19,597–19,619.

Hajash, A., and G. W. Chandler (1981), An experimental investigation of high-temperature interactions between seawater and rhyolite, andesite, basalt and peridotite, *Contrib. Mineral. Petrol.*, *78*, 240–254.

Heaman, L. M., R. Bowins, and J. Crockett (1990), The chemical composition of igneous zircon suites: Implications for

geochemical tracer studies, *Geochim. Cosmochim. Acta*, *54*, 1597–1607.
Holland, H. D. (1978), *The Chemistry of the Atmosphere and Oceans*, 351 pp., John Wiley, Hoboken, N. J.
Humphris, S. E., and G. Thompson (1978), Trace element mobility during hydrothermal alteration of oceanic basalts, *Geochim. Cosmochim. Acta*, *42*, 127–136.
Janecky, D. R., and W. E. Seyfried Jr. (1986), Hydrothermal serpentinization of peridotite within the oceanic crust: Experimental investigations of mineralogy and major element chemistry, *Geochim. Cosmochim. Acta*, *50*, 1357–1378.
Johannes, W. (1969), An experimental investigation of the system $MgO\text{-}SiO_2\text{–}H_2\text{–}O_2\text{–}CO_2$, *Am. J. Sci.*, *267*(9), 1083–1104.
Karson, J. A. (1990), Seafloor spreading on the Mid-Atlantic Ridge: Implications for the structure of ophiolites and oceanic lithosphere produced in slow-spreading environments, in *Ophiolites and Oceanic Crustal Analogues: Proceedings of the Symposium "Troodos 1987,"* edited by J. Malpas et al., pp. 125–130, Geol. Surv. Dep., Nicosia, Cyprus.
Karson, J. A. (1998), Internal structure of oceanic lithosphere: A perspective from tectonic windows, in *Faulting and Magmatism at Mid-ocean Ridges*, *Geophys. Monogr. Ser.*, vol. 106, edited by W. R. Buck et al., pp. 177–218, AGU, Washington, D. C.
Karson, J. A. (1999), Geological investigation of a lineated massif at the Kane transform: Implications for oceanic core complexes, *Philos. Trans. R. Soc. London, Ser. A*, *357*, 713–740.
Karson, J. A., and H. J. B. Dick (1983), Tectonics of ridge-transform intersections at the Kane Fracture Zone, *Mar. Geophys. Res.*, *6*, 51–98.
Karson, J. A., and R. M. Lawrence (1997), Tectonic setting of serpentinite exposures on the western median valley wall of the MARK Area in the vicinity of Site 920, *Proc. Ocean Drill. Program Sci. Results*, *153*, 5–22.
Karson, J. A., M. Cannat, D. J. Miller, and D. Elthon (Eds.) (1997), *Proceedings of the Ocean Drilling Program, Science Results*, vol. 153, Ocean Drill. Program, College Station, Tex.
Kelemen, P. B., et al. (2004), *Proceedings of the Ocean Drilling Program*, *Initial Reports* [CD-ROM], vol. 209, Ocean Drill. Program, College Station, Tex.
Kelley, D. S., K. M. Gillis, and G. Thompson (1993), Fluid evolution in submarine magma-hydrothermal systems at the Mid-Atlantic Ridge, *J. Geophys. Res.*, *98*, 19,579–19,596.
Kelley, D. S., et al. (2001), An off-axis hydrothermal vent field near the Mid-Atlantic Ridge at 30°N, *Nature*, *412*, 145–149.
Kelley, D. S., et al. (2005), A serpentinite-hosted ecosystem: The Lost City Hydrothermal Field, *Science*, *307*, 1428–1434.
King, R. L., M. J. Kohn, and J. M. Eiler (2003), Constraints on the petrologic structure of the subduction zone slab-mantle interface from Franciscan Complex exotic ultramafic blocks, *Geol. Soc. Am. Bull.*, *115*(9), 1097–1109.
Klinkhammer, G. P., H. Elderfield, J. Edmond, and A. Mitra (1994), Geochemical implications of rare earth element patterns in hydrothermal fluids from mid-ocean ridges, *Geochim. Cosmochim. Acta*, *58*, 5105–5113.
Leake, B. E. (1978), Nomenclature of amphiboles, *Am. Mineral.*, *63*, 1023–1052.
MacLeod, C. J., et al. (2002), Direct geological evidence for oceanic detachment faulting: The Mid-Atlantic Ridge, 15°45′N, *Geology*, *30*, 879–882.
McDonough, W. F., and S. S. Sun (1995), The composition of the Earth, *Chem. Geol.*, *120*, 223–253.
Mercier, J.-C. C., and A. Nicolas (1975), Textures and fabrics of upper-mantle peridotites as illustrated by xenoliths from basalts, *J. Petrol.*, *16*(2), 454–487.
Michard, A., F. Albarede, G. Michard, J. F. Minster, and J. L. Charlou (1983), Rare-earth elements and uranium in high-temperature solutions from East Pacific Rise hydrothermal vent field (13°N), *Nature*, *303*, 795–797.
Miller, R. B. (1988), Fluid flow, metasomatism and amphibole deformation in an imbricated ophiolite, North Cascades, Washington, *J. Struct. Geol.*, *10*, 283–296.
Miyashiro, A. (1973), *Metamorphism and Metamorphic Belts*, John Wiley, Hoboken, N. J.
Miyashiro, A., F. Shido, and K. Kanehira (1979), Metasomatic chloritization of gabbros in the Mid-Atlantic Ridge near 30°N, *Mar. Geol.*, *31*, M47–M52.
Moore, D. E., D. A. Lockner, M. Shengli, R. Summers, and J. D. Byerlee (1997), Strengths of serpentinite gouges at elevated temperatures, *J. Geophys. Res.*, *102*(B7), 14,787–14,801.
Moores, E. M., P. T. Robinson, J. Malpas, and C. Xenophontos (1984), Model for the origin of the Troodos Massif, Cyprus, and other Mideast ophiolites, *Geology*, *12*(8), 500–503.
Müller, W. F., E. Schmadicke, M. Okrusch, and U. Schüssler (2003), Intergrowths between anthophyllite, gedrite, calcic amphibole, cummingtonite, talc and chlorite in a metamorphosed ultramafic rock of the KTB pilot hole, Bavaria, *Eur. J. Mineral.*, *15*, 295–307.
Mutter, J. C., and J. A. Karson (1992), Structural processes at slow-spreading ridges, *Science*, *257*, 627–634.
Nesbitt, R. W., E. Pascual, C. M. Fanning, M. Toscano, R. Saez, and G. R. Almodovar (1999), U-Pb dating of stockwork zircons from the eastern Iberian pyrite belt, *J. Geol. Soc. London*, *156*(1), 7–10.
Nooner, S. L., G. S. Sasagawa, D. K. Blackman, and M. A. Zumberge (2003), Structure of oceanic core complexes: Constraints from seafloor gravity measurements made at the Atlantis Massif, *Geophys. Res. Lett.*, *30*(8), 1446, doi:10.1029/2003GL017126.
O'Hanley, D. S. (1996), *Serpentinites*, 277 pp., Oxford Univ. Press, New York.
Palandri, J. L., and M. H. Reed (2004), Geochemical models of metasomatism in ultramafic systems: Serpentinization, rodingitization, and sea floor carbonate chimney precipitation, *Geochim. Cosmochim. Acta*, *68*(5), 1115–1133.
Passchier, C. W., and R. A. J. Trouw (1998), *Micro-tectonics*, 289 pp., Springer, New York.
Penrose Conference Participants (1972), Penrose field conference on ophiolites, *Geotimes*, *17*, 24–25.
Ranero, C. R., and T. J. Reston (1999), Detachment faulting at ocean core complexes, *Geology*, *27*, 983–986.
Reston, T. J., et al. (2002), A rifted inside corner massif on the Mid-Atlantic Ridge at 5°S, *Earth Planet. Sci. Lett.*, *200*, 255–269.
Reynolds, S. J., and G. S. Lister (1987), Structural aspects of fluid-rock interactions in detachment zones, *Geology*, *15*, 362–366.
Rubin, J. N., C. D. Henry, and J. G. Price (1993), The mobility of zirconium and other "immobile" elements during hydrothermal alteration, *Chem. Geol.*, *110*, 29–47.
Schroeder, T., and B. E. John (2004), Strain localization on an oceanic detachment fault system, Atlantis Massif, 30°N, Mid-Atlantic Ridge, *Geochem. Geophys. Geosyst.*, *5*, Q11007, doi:10.1029/2004GC000728.
Stakes, D., C. Mével, M. Cannat, and T. Chaput (1991), Metamorphic stratigraphy of Hole 735B, *Proc. Ocean Drill. Program Sci. Results*, *118*, 153–180.

Talbi, E. H., J. Honnorez, N. Clauer, F. Gauthier Lafaye, and P. Stille (1999), Petrology, isotope geochemistry and chemical budgets of oceanic gabbros-seawater interactions in Equatorial Atlantic, *Contrib. Mineral. Petrol.*, *137*(3), 246–266.

Taylor, B., and P. Huchon (2002), Active continental extension in the western Woodlark Basin: A synthesis of Leg 180 results, *Proc. Ocean Drill. Program Sci. Results*, *180*, 1–36.

Taylor, B., et al. (1999), Active continental extension in the western Woodlark Basin, Papua New Guinea, *Proc. Ocean Drill. Program Initial Rep.*, *180*, 1–35.

Tenthorey, E., and S. F. Cox (2003), Reaction-enhanced permeability during serpentinite dehydration, *Geology*, *31*(10), 921–924.

Tucholke, B. E., J. Lin, and M. C. Kleinrock (1998), Megamullions and mullion structure defining oceanic metamorphic core complexes on the Mid-Atlantic Ridge, *J. Geophys. Res.*, *103*, 9857–9866.

Tucholke, B. E., K. Fujioka, T. Ishihara, G. Hirth, and M. Kinoshita (2001), Submersible study of an oceanic megamullion in the central North, *J. Geophys. Res.*, *106*, 16,145–16,161.

Vanko, D. A., and D. Stakes (1991), Fluids in oceanic layer 3: Evidences from veined rocks, Hole 735B, Southwest Indian Ridge, *Proc. Ocean Drill. Program Sci. Results*, *118*, 181–215.

Wernicke, B. (1981), Low-angle normal faults in the Basin and Range province: Nappe tectonics in an extending orogen, *Nature*, *291*, 645–648.

Wetzel, L. R., and E. L. Shock (2000), Distinguishing ultramafic- from basalt-hosted submarine hydrothermal systems by comparing calculated vent fluid compositions, *J. Geophys. Res.*, *105*(B4), 8319–8340.

Wick, F. J., and E. J. W. Whittaker (1977), Serpentine textures and serpentinization, *Can. Mineral.*, *15*, 459–488.